Flexible and Interpretable Generalization of Self-Evolving Computational Materials Framework

Mohammed Bazroun¹, Yicheng Yang¹, and In Ho Cho^{1,2}

4 ABSTRACT

The recent innovations of computational material models by machine learning (ML) methods face
formidable challenges. Incorporating internal heterogeneity and diverse boundary conditions
(BC's) into existing ML methods remains difficult, and the weak interpretability of ML remains
unresolved. To tackle these challenges, this paper generalizes a recently developed self-evolving
computational material models framework built upon Bayesian update and evolutionary algorithm.
This paper proposes a new material-specific information index (II), which is capable of
autonomously quantifying the internal heterogeneity and diverse BC's. Also, this paper introduces
highly flexible cubic regression spline (CRS)-based link functions which can offer mathematical
expressions of salient material coefficients of the existing computational material models in terms
of convolved II. Thereby, this paper suggests a novel means by which ML can directly leverage
internal heterogeneity and diverse BC's to autonomously evolve computational material models
while keeping interpretability. Validations using a wide spectrum of large-scale reinforced
composite structures confirm the favorable performance of the generalization. Example
expansions of nonlinear shear of quasi-brittle materials and progressive compressive buckling of
reinforcing steel underpin efficiency and accuracy of the generalization. This paper adds a
meaningful avenue for accelerating the fusion of computational material models and ML.

Keywords: Evolutionary algorithm; cubic regression spline; computational material model; machine learning for heterogeneity; machine learning for varying boundary conditions; nonlinear analysis of reinforced concrete structures

¹ Department of Civil, Construction and Environmental Engineering, Iowa State University, Ames, IA 50011, USA.

² E-mail address: <u>icho@iastate.edu</u>; Corresponding author.

1. Introduction

25

26

27

28

29

30

31

32

33

34

35

36

37

38

39

40

41

42

43

44

45

46

47

Traditionally, computational material models are derived from well-designed experiments and statistical fitting (Fig. 1B). Owing to their fascinating learning power of complex data, machine learning (ML) methods have attracted researchers in computational mechanics and structures over the past decades. Researchers apply ML to constitutive rules at the material point level (Fig. 1C). This paper denotes such attempts as an "ML-driven" approach. For instance, Hashash et al. [1] derived the consistent material stiffness matrix for constitutive model using a standard multi-layer feed-forward neural network. Koenuma et al. [2] used deep learning to understand aluminum alloy sheets' deformation behavior. Vlassis et al. [3] performed a hybrid ML approach that combines an unsupervised graph convolutional neural network, which uses Sobolev training to fit target output values as well as derivatives. Logarzo et al. [4] developed a recurrent neural networks-based constitutive model to handle sequence-to-sequence data, including the deformation histories, stress histories, and the fading gradient effect. Masi et al. [5] proposed a neural network model that is physics-based and thermodynamics-based artificial neural networks. The model uses the recurrent neural network for modeling path-dependent plasticity models. On the other hand, some apply ML methods to the global structural level (Oh et al. [6]; Okazaki et al. [7]; Wu and Jahanshahi [8]; Cladera and Mari [9]; Tehranizadeh and Safi [10]). In particular, Abdalla et al. [11] adopted an artificial neural network (ANN) for predicting the shear resistance of reinforced beam. Abdalla et al. [12] used ANN to predict the optimum design parameters of unbonded post-tensioned coupled precast concrete wall systems. Abundeh et al. [13] studies the shear deficient reinforced concrete beams connected with fiber-reinforced polymers laminates using the resilient back-propagating neural network, the neural interpretation diagrams, and the recursive feature elimination. Solhmirzaei et al. [14] used support vector machine, k-nearest neighbor, and ANN for classifying the failure mode of ultra-high-performance concrete beams and then used genetic programming for deriving an expression of the beams' shear capacity. Table B.1 in the appendix summarizes some global structural level applications of ML methods in more detail.

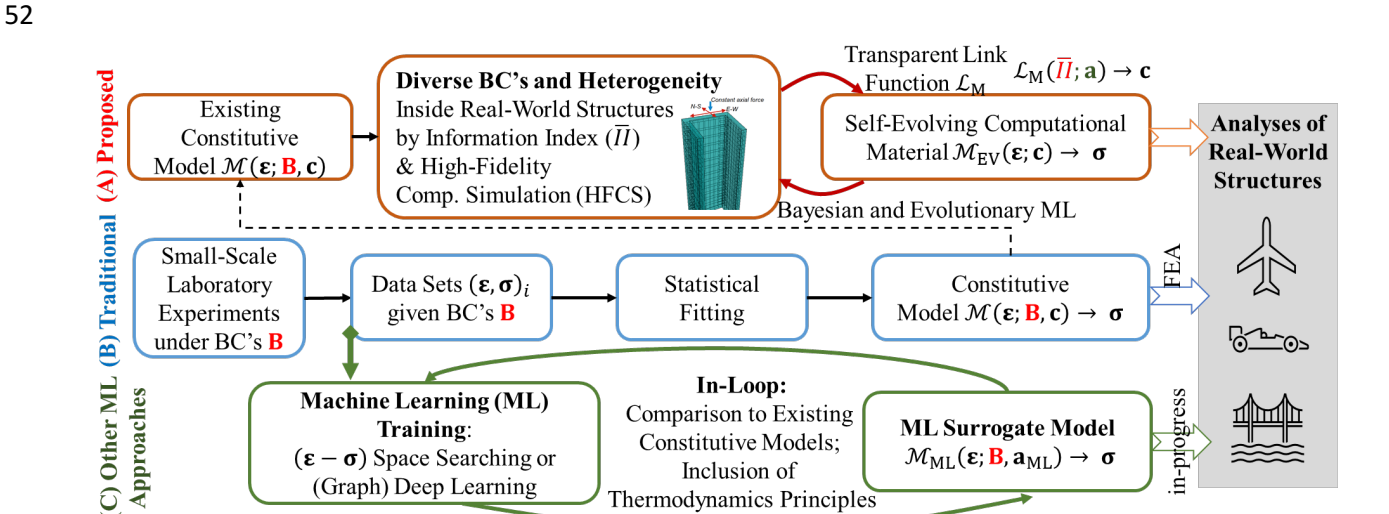


Fig. 1. A schematic comparison of (A) the proposed glass-box computational material framework, (B) the traditional approach to constitutive rule derivation, and (C) the recent ML-based approaches.

Another notable mainstream is to directly use experimental or simulation data for describing material behaviors. This paper denotes this attempt as a "data-driven" approach since their focus lies indirect route between data and material behavior, sometimes bypassing any form of constitute rules. For instance, Bessa et al. [15] developed a new data-driven computational framework for ML to help design new material systems and structures by three steps of designing experiments, computational analysis to create the material response database, and ML through a feedforward network. Ma and Pan [16] presented a data-driven nonintrusive model order reduction method for dynamical systems with moving boundaries by combining three techniques: proper orthogonal decomposition, Gaussian process regression, and moving least squares interpolation. Inspired by the initial work of Kirchdoerfer and Ortiz [17], Eggersmann et al. [18] extended the data-driven

computing paradigm by combining locally linear tangent spaces into the data set. Patel et al. [19] presented a regression framework for finding continuum models from high fidelity molecular simulation data based on a neural network parameterization of governing physics in modal space. Despite their meaningful contributions to our understanding of materials and structures, there are two critical challenges, the lack of interpretability and the limited description of the internal complexity of heterogeneous materials and diverse boundary conditions (BC's). The weak interpretability issue is rooted in the ML method's nature, and the incomplete description of internal complexity and BC's are inherited from data, the starting point of training and learning. In terms of the first challenge of interpretability, most of the existing ML-driven approaches to material models and structures rarely offer detailed explanations behind the input-output relations, thereby rendering them a "black-box" approach. This limit is considered a severe disadvantage in practical applications (Cheng et al. [20]). Therefore, it is of critical importance to develop a "glassbox" approach (as opposed to the black-box) that can help unravel the hidden relation between input and output engineering data. As regards the second challenge of incomplete data, both datadriven and ML-driven approaches essentially rely upon training data which are obtained from small-scale laboratory tests under specific BC's to come up with a sort of surrogate model representing or replacing the constitutive model (Fig. 1C). In advanced settings, material heterogeneity is also included for small experiments or computational simulations for training data generation. For instance, Mozaffar et al. [21] used the recurrent neural network for finding history and microstructure-dependent constitutive models for the homogenized stresses and plastic energy of heterogeneous materials. Abueidda et al. [22] developed convolutional network models to obtain new optimum materials considering linear elastic or hyperplastic materials. These models were based on the topology optimization and the ResUnet method, which is a convolutional neural

68

69

70

71

72

73

74

75

76

77

78

79

80

81

82

83

84

85

86

87

88

89

network aimed to get high performance with fewer parameters. Chen and Gu [23] presented a framework based on deep neural networks to obtain and design a novel composite material. Abueidda et al. [24] presented a sequence learning model that can predict the entire path-dependent for a periodic elastoplastic material using different recurrent neural network architectures such as long short-term memory and gated recurrent unit. Kollmann et al. [25] developed a convolutional neural network (CNN) model based on the ResUnet method presenting a noniterative topology optimization of metamaterials. However, there exists an intrinsic discrepancy between reality and physical or computational experiments. Inside the real-world structures, substantially diverse BC's and material heterogeneity exist, and the training data sets can hardly encompass the entire spaces of all possible physical conditions. To overcome the critical challenges, this work adopts and generalizes a "glass-box" computational material model framework (Fig. 1A) developed by Cho [26] (in short, glass-box framework hereafter). The central novelty of the glass-box framework is twofold. First, it can combine basic physics principles and spatial convolution (a salient driving force of deep learning) to generate convolved information index (II) so that ML autonomously perceives internal heterogeneity and complex BC's within real-world structures. Second, the glass-box framework offers room for transparent link functions (LF's) that can unravel hidden rules behind the material coefficients of adopted computational material mechanisms. The convolved II can put scientists' eyes onto ML and see through a complex physical system imbued with heterogeneity and diverse BC's; LF's can help unravel the hidden relations between the convolved II and mechanisms. Still, in the initial work, the glass-box framework accommodates two material models with a simple two-parameter exponential form LF, which necessitates substantial generality, flexibility, and expandability for broader applicability. This paper generalizes the glass-box framework by

91

92

93

94

95

96

97

98

99

100

101

102

103

104

105

106

107

108

109

110

111

112

proposing a set of new convolved II's essential for the extension to additional material mechanisms. This paper describes how to develop new convolved II tailored for new additional material mechanisms, and the example extended mechanisms include the nonlinear shear of cracked quasi-brittle materials and reinforcing steel's progressive buckling mechanisms. Importantly, this paper explains how to honor and infuse the existing material mechanisms onto the glass-box framework. Also, this paper generalizes the glass-box framework by including the cubic regression spline (CRS) (Hastie and Tibshirani [27]; Wood [28]). The CRS-based LF can simultaneously describe constant shift, linear, and highly nonlinear relationships since it mathematically contains all these relations in terms of simple bases. CRS-based LF's successfully help unravel the hidden rules about strength enhancement, nonlinear shear strength degradation, and the progressive buckling phenomena. As illustrated in Fig. 1A, the proposed glass-box framework leverages existing constitutive model at integration (material) points on an implicit FEA platform but seeks to replace decisive material coefficients of the constitutive model with the machine learning-identified rules, thereby engendering "evolving" constitutive models. This paper is organized as follows. Section 2 summarizes and gives a general idea about the adopted glass-box framework. Section 3 presents a new convolved II that is tailored for new material models related to the smart bar's progressive buckling phenomena. Section 4 derives a flexible and transparent expression of a hidden relation between convolved II and computational material's coefficients by using CRS-based LF. Section 5 revisits existing computational material models that are used for demonstrating the extensibility of the glass-box framework. Section 6 presents feasibility test settings to show the framework's positive impacts with a wide spectrum of large-scale reinforced composite structures. Section 7 discusses the results from the feasibility test and shows the accuracy of the proposed framework.

114

115

116

117

118

119

120

121

122

123

124

125

126

127

128

129

130

131

132

133

134

135

2. Revisit to the glass-box computational material framework

2.1. Overall flow of glass-box framework

As schematically illustrated in Fig. 2, there are notable analogies between the adopted glass-box framework and the convolutional neural network (CNN), a popular deep learning method. In both, convolution is used for learning and prediction with complex data sets. The generation of convolved II of the glass-box framework is similar to the convolution and pooling of CNN in the sense that both can provide a spatially weighted averaging to collect information from adjacent regions and come up with new information measures. In lieu of error backpropagation of CNN, the global fitness of the unraveled rules is used for the next-generation products in the evolutionary algorithm. While in CNN, each neuron's weight and activation function describe the nonlinear relationship (still opaque), the glass-box framework seeks to find transparent (i.e., in terms of expression) rule via LF at each material point.



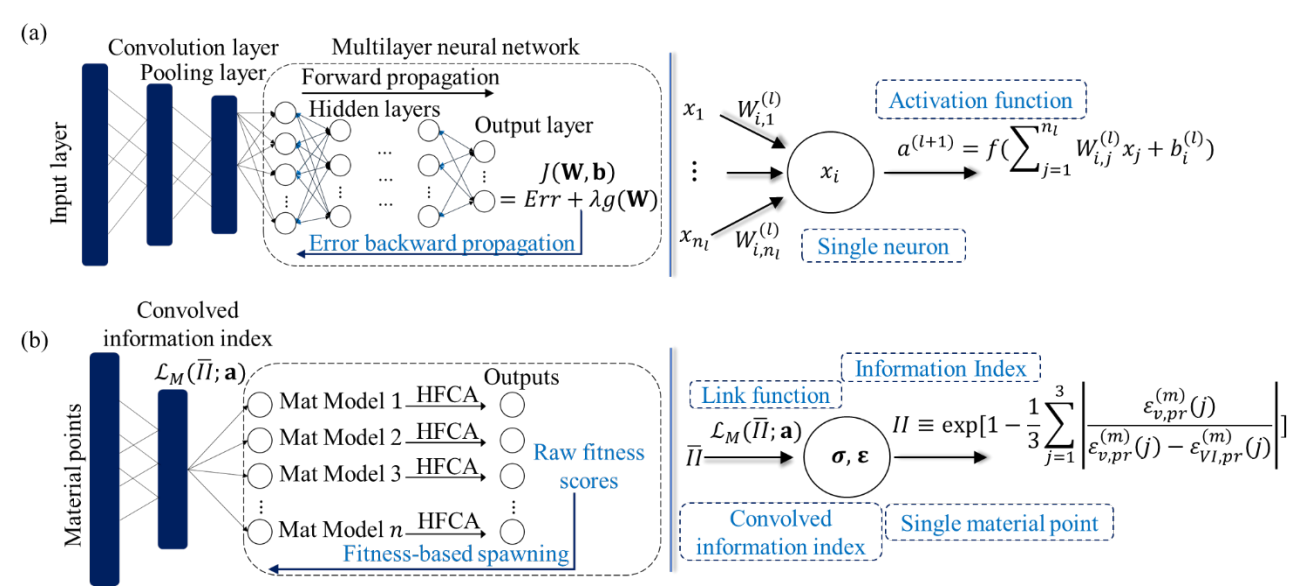


Fig. 2. A high-level analogy between the typical convolutional neural network (CNN) and the glass-box framework: (a) a typical single neuron of CNN; (b) the glass-box framework's an individual material point which is the counterpart to the single neuron of CNN. $W_{i,j}^{(l)}$ is the weight in layer (*l*) from neuron *j* to *i*; f(.) is an activation function; $b_i^{(l)}$ is the bias term.

Fig. 3 shows the self-evolving nature of the glass-box framework in which the Bayesian update plays in concert with the evolutionary algorithm, a genetic algorithm (GA) herein. With new specimens, convolved II guides the ML method to internal heterogeneity and BC's at the material point level. Then, multiple LF's of multiple computational material models interact within the loops of generations and organisms in GA and high-fidelity computational simulation platform (HFCS) for typical selection, spawning, and evolution of GA. LF's can understand the hidden relations between convolved II and a computational material model (denoted as M). Finally, to strengthen the best-so-far LF, new experimental data of different test systems are used by Bayesian updates with the prior best of the LF.

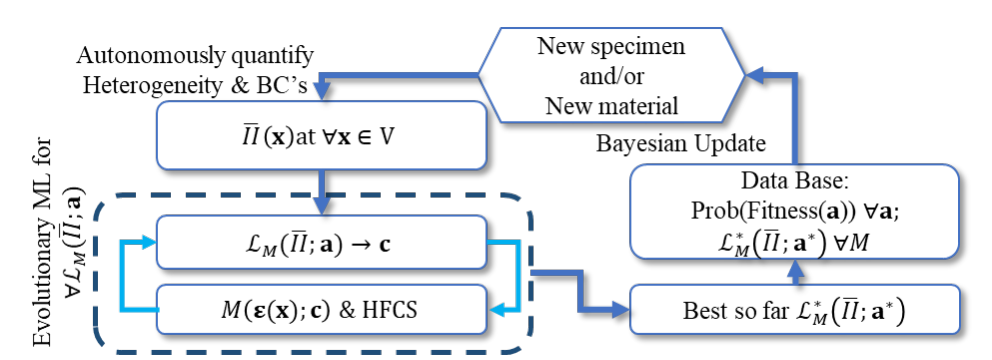


Fig. 3. The overall flow of the self-evolving nature of the glass-box computational materials framework. $\overline{\Pi}(\mathbf{x}) = \text{convolved}$ information index; V = the domain; $\mathcal{L}_M = \text{link function}$; $\mathbf{c} = \text{target}$ coefficients of adapted computational materials; $M(\boldsymbol{\varepsilon}(\mathbf{x}); \boldsymbol{c}) = \text{a computational material model}$; HFCS = high-fidelity computational simulation platform; $\mathcal{L}_M^* = \text{best-so-far link function}$.

In terms of creating the next generation of GA, there are many evolution methods about GA in the literature (Wang et al. [29]; Tang et al. [30]; Johnson and Rahmat-Samii [31]; Waisman et al. [32]; Koza [33]). The adopted glass-box framework uses the fitness-proportionate probability (FPP) to ease Bayesian update, in which the probability of an organism *s* in the recent generation is selected as a new parent for the next generation. A detailed explanation is presented in Cho [26]. Here, a central idea is summarized. In general, prior knowledge is the collected information obtained from

earlier validations using different specimens. In the beginning, an initial unknown distribution of parameter \mathbf{a} is signified as $\pi(\mathbf{a})_{prior} = p(\mathbf{a}|\mathcal{L}_M)$ where $p(\mathbf{a}|\mathcal{L}_M)$ is the probability density function (PDF) of a set of free parameters \mathbf{a} for an LF \mathcal{L}_M related to a material model M. Then, the Bayesian update of LF's can be obtained by

183
$$\pi(\mathbf{a})_{posterior} = p(\mathbf{a} | \pi(\mathbf{a})_{prior}, \mathcal{L}_M) = \frac{p(\pi(\mathbf{a})_{prior} | \mathbf{a}, \mathcal{L}_M) p(\mathbf{a} | \mathcal{L}_M)}{p(\pi(\mathbf{a})_{prior} | \mathcal{L}_M)}$$
(1)

where $p(\pi(\mathbf{a})_{prior}|\mathcal{L}_M) = \int p(\pi(\mathbf{a})_{prior})p(\mathbf{a}|\mathcal{L}_M) d\mathbf{a}$. After that, using different specimens creates new \mathbf{a} and $\pi(\mathbf{a})_{posterior}$ to serve as $\pi(\mathbf{a})_{prior}$ for the next update. It should be noted that the Bayesian update is performed through the detected fitness distributions instead of assuming an artificial distribution of $\pi(\mathbf{a})$. In detail, completing a full GA throughout whole generations can lead to the best generation and organism that contains the largest fitness score. The prior best generation's fitness score $\mathcal{F}^*(s;\mathcal{L}_M)$ is combined with the current fitness scores $\mathcal{F}(s;\mathcal{S}^*(\mathbf{a}),\mathcal{L}_M)$ where $\mathcal{S}^*(\mathbf{a})$ is the set of \mathbf{a} of the prior best generation. Also, based on the FPP rule, the Bayesian fitness score of an individual new organism $\mathcal{F}_B(s;\mathcal{L}_M)$, $s=1,\ldots,M_{org}$, can be obtained by

192
$$\mathcal{F}_B(s; \mathcal{L}_M) = \frac{1}{k} \frac{\mathcal{F}(s; S^*(\mathbf{a}), \mathcal{L}_M) \mathcal{F}^*(s; \mathcal{L}_M)}{\sum_{\forall s} \mathcal{F}^*(s; \mathcal{L}_M)}$$
(2)

193 where

$$k = \sum_{\forall s} \frac{\mathcal{F}(s; S^*(\mathbf{a}), \mathcal{L}_M) \mathcal{F}^*(s; \mathcal{L}_M)}{\sum_{\forall s} \mathcal{F}^*(s; \mathcal{L}_M)}$$
(3)

2.2. Convolved information index

The II is used to give ML the ability to learn and improve the unknown of a material model and use it in LF. The main goal of convolved II is to autonomously determine the laboratory-reality similarity, i.e., complex heterogeneity and diverse BC's inside the physical system. There is no limit to derive domain-specific II, and there is ample room to incorporate engineering principles

or basic mechanics for the desired physical information. Cho [26] presented an efficient derivation that uses "virtual stress" at material points, which provides a new feature to each material point to make ML methods understand the physical system. This virtual stress-based II is defined as

204
$$II = \exp\left[1 - \frac{1}{3} \sum_{j=1}^{3} \left| \frac{\varepsilon_{v,pr}^{(m)}(j)}{\varepsilon_{v,pr}^{(m)}(j) - \varepsilon_{VI,pr}^{(m)}(j)} \right| \right]$$
(4)

where $II \in \mathbb{R}[0,1]$. $\varepsilon_{VI,pr}^{(m)}$ and $\varepsilon_{v,pr}^{(m)}$ correspond to realistic deformation inside the real system and the free deformation under the virtual stress σ_V , respectively. As shown in Fig. 4, this new II can help internal material points "feel" adjacent heterogeneity as well as general BC's. This virtual stress-based II quantifies the degree of proximity to nearby stiff materials or BC's with a single scalar value within [0, 1]. The full derivation of this virtual stress-based II is presented in Appendix C.

As another example of II, it can be derived by using gravity (i.e., self-weight of the structure) (Cho and Hall [34]). This gravity-based II was defined in terms of compression induced lateral strains ε_{li} as

214
$$II = \begin{bmatrix} 1 - d & \text{Linear form} \\ 1/\exp(d) & \text{Exponential form} \end{bmatrix}$$
 (5)

where d is an intermediate-term, and it can be obtained as

$$d = \frac{1}{2} \left(\frac{\langle \varepsilon_1 \rangle_+}{\varepsilon_{l1}} + \frac{\langle \varepsilon_2 \rangle_+}{\varepsilon_{l2}} + \frac{\langle \varepsilon_3 \rangle_+}{\varepsilon_{l3}} \right) \tag{6}$$

where ε_i is the strain in the *i*th principal direction; $x_+ = x$ for x > 0 and $x_+ = 0$ for $x \le 0$. This choice of gravity was successful in quantifying the complex reinforcement layout.

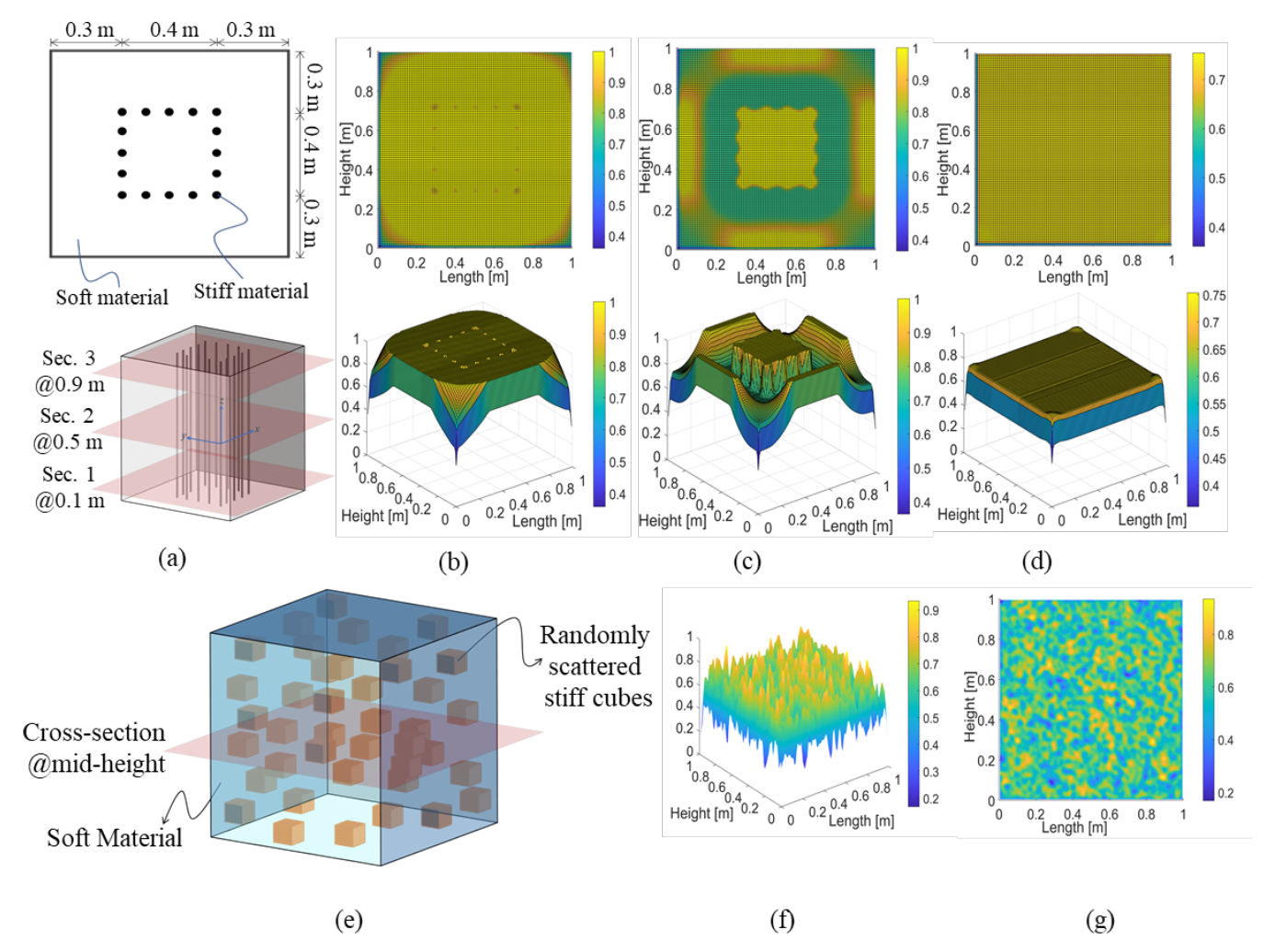


Fig. 4. Example plots of II: (a) \sim (d) birds-eye (bottom row) and plan view (top row); (a) real-scale composite structure with dimensions of $(1m \times 1m \times 1m)$ containing 16 steel bars; (b) the convolved II distribution on the horizontal cross-section 1, (c) on the horizontal cross-section 2, and (d) on the horizontal cross-section 3. The vertical axis corresponds to the convolved II; (e) a view of randomly scattered stiff small cubes with dimensions each of $(0.01m \times 0.01m \times 0.01m)$ inside a soft body with dimensions of $(1m \times 1m \times 1m)$. The random cubes' stiffness is $(10^2, 10^3, 10^4)$ times greater than that used in the soft material; (f) convolved II distribution confirms the proximity of the stiff cubes; (g) plan view of convolved II at the cross-section.

Both of these two II's can effectively quantify the realistic proximity to stiff reinforcements and firmly fixed bottom. However, the key difference between them is that the virtual stress-based II has no dependency on gravity direction and thus rotation-invariant. The gravity-based II is easy to implement, but by nature, it is dependent upon the direction of self-weight. Thus, throughout this paper, we used the virtual stress-based II for all the subsequent formulations and feasibility tests.

With the virtual stress-based II (Eq. 4), the spatial convolution has been conducted by

$$\overline{II}(\mathbf{x}) = \int \omega(\mathbf{x}, \boldsymbol{\xi}) \, II(\boldsymbol{\xi}) d\boldsymbol{\xi} \tag{7}$$

where $\omega(r)$ can represent the Gaussian weighting function, and it can be defined as

240

241

242

243

244

245

246

247

248

249

250

251

252

253

254

255

256

257

$$\omega(r) = \left(L\sqrt{2\pi}\right)^{-N} \exp\left(-\frac{r^2}{2L^2}\right) \tag{8}$$

where N = 3; L is the influence range; r is the spatial distance and can be defined as $r = |\mathbf{x} - \boldsymbol{\xi}|$;

x is the position vectors; ξ is the integration point location vector (Bazant and Jirasek [35]; Cho and Hall [34]). Fig. 4a-d show how the convolved II can feel the proximity to the fixed bottom boundary (Fig. 4b) and free top boundary (Fig. 4d). Also, Fig. 4c shows how the convolved II can inform material points with stiff embedded bars (Fig. 4c). Figs. 4e-g show how the convolved II can help material points feel the adjacent stiff (heterogeneous) materials and can perceive the randomly distributed heterogeneous small volumes. All of these "perception" is autonomously done. As proven in Cho [26], the favorable properties of the virtual stress-based II include the invariance to the external tractions (e.g., pressures or gravity), rotation, or translation. The convolved II is only affected by the physical proximity to adjacent materials and BC's. This invariance is critical and cannot be achieved by the use of principal stresses. For instance, Fig. 5a shows separate simulations of a stiff bucket filled with soft material with varying gravity and pressures. Fig. 5b and Fig. 5c show the maximum principal stress on the soft material's mid-height with gravity in the Y- and X-direction, respectively. Fig. 5d and Fig. 5e show the maximum principal stress under vertical pressure of 10 KPa and 100 KPa, respectively. Unlike these principal stresses, the current virtual stress-based convolved II is completely independent of gravity directions, external tractions (i.e., all plots of Fig. 4 are independent of external tractions or gravity).

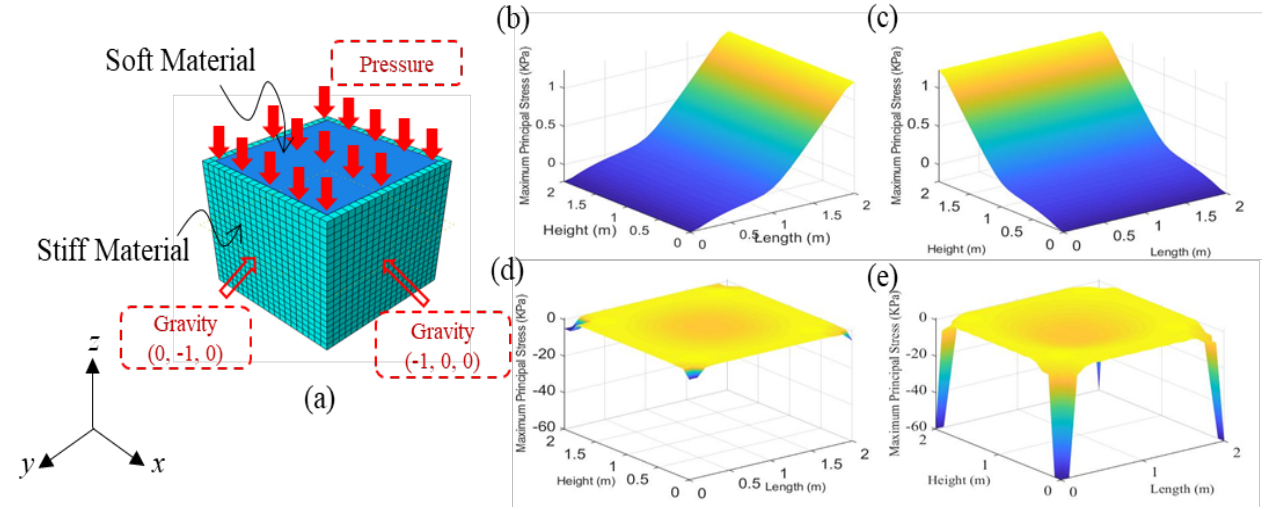


Fig. 5. Example plots of principal stress-based II and each dependency on the gravity direction: (a) the insight of a soft material in a stiff bucket with dimensions of $(2m \times 2m \times 2m)$; (b) the maximum principal stress on the mid-height of the soft material with gravity on y-direction; (c) the maximum principal stress on the mid-height of the soft material with gravity on x-direction; (d) the maximum principal stress for a pressure of 10 KPa on z-direction; (e) the maximum principal stress for a pressure of 100 KPa on z-direction.

3. New convolved II tailored for a smart bar model's progressive buckling

This section elaborates on how the convolved II concept can be applied to an existing computational material model. As an example, a new convolved II is proposed to help evolutionary ML autonomously improves decisive material coefficients of a complex progressive reinforcing steel bar buckling model. Under excessively repeated loadings, reinforcing steel bar exhibits progressive buckling behavior, which is highly challenging to capture by experimental efforts (Rodriquez et al. [36]; Dhakal and Maekawa [37]). The computational bar model is denoted as the "smart" bar model (Cho [38]) since it leverages internal topological information such as bar connectivity and damage states of surrounding brittle materials.

Recalling the fundamental limit of the traditional experiment-based derivation (Fig. 1B) of the computational material model, the formulations about the progressive buckling are likely to depend on simplified assumptions such as fixed-end BC's of a bare bar without interaction with

surrounding heterogeneous materials. In the smart bar model, the onset of compressive buckling is expected when all the surrounding brittle material's elements enter at least a partially crushed state. Therefore, to evaluate the energy state of the material, two internal state variables are considered. First, the internal state variable at the integration point level $\alpha_i^{(k)}$ describes uncrushed state by 1 and crushed state by 2

$$\alpha_i^{(k)} = \begin{cases} 1 & \text{for min } \varepsilon_k^{cr} > \varepsilon_{th} \\ 2 & \text{otherwise} \end{cases}$$
 (9)

where k is the crack surface $\in \{1,2,3\}$; ε_{th} is the strain threshold for entering the crush phase, which is assumed to be the strain associated with the compressive strength. Second, the internal state variable at the element level, which can be denoted as λ_j , can show intact, partially crushed, and fully crushed states of an element using simple integer values such as 0, 1, and 2, respectively.

289
$$\lambda_{j} = \begin{cases} 0 & \beta_{j} \leq \text{NINT}^{(j)} \times 3 \\ 1 & \text{NINT}^{(j)} \times 3 < \beta_{j} \leq \text{NINT}^{(j)} \times 6 \\ 2 & \beta_{j} > \text{NINT}^{(j)} \times 6 \end{cases}$$
(10)

where NINT^(j) is the number of integration points of the jth element \in surrounding element S_m ;

291
$$\beta_j = \sum_{i=1}^{\text{NINT}^{(j)}} \sum_{k=1}^3 \alpha_i^{(k)}$$
 (11)

The topological transition is assumed to take place if all surrounding elements enter the partially crushed phase, which can be determined by

$$\sum_{j=1}^{n(S_m)} \lambda_j \ge n(S_m) \tag{12}$$

where $n(S_m)$ is the number of surrounding elements in S_m . Hence, once the above condition is confirmed, the onset of buckling can be obtained by proposing a new convolved II of the bar, denoted as $\overline{\Pi}_b$ where $\overline{\Pi}_b \in \mathbb{R}[0,1]$ and it can be defined as

298
$$\overline{II}_{b}(t) = \frac{1}{n(S_{m})} \sum_{i=1}^{NINT} \sum_{j=1}^{n(S_{m})} \left[\frac{\overline{II}(i)}{3 \cdot NINT} + \frac{2 - \lambda(t)}{3} \right]^{(j)}$$
(13)

300

301

302

303

304

305

306

307

308

309

310

311

312

313

314

315

316

Where $\overline{II}(i)$ is the convolved II at the *i*th integration point; $\frac{\overline{II}(i)}{NINT}$ is the average convolved II of *j*th element material; $\lambda(t)$ is the damage state of *j*th brittle element material at time t; the values 2 and 3 are used for scaling. In Eq. 13, \overline{II}_b can collect the adjacent information presented by the convolved II and the damage states by summation over all integration points (i.e., NINT) of all associated $n(S_m)$ surrounding elements since the current surrounding brittle material's status affects the buckling of the reinforcing steel. For example, when the average convolved II is 0 (free to deform), and the brittle material is fully crushed (i.e., $\lambda(t) = 2$), there will be no impact from the surrounding brittle material on the reinforcement bar; hence, $\overline{II}_b = 0$. However, when the convolved II is 1 (almost fixed), and the brittle material is intact ($\lambda(t) = 0$), the brittle material will not allow buckling on the reinforcement bar; hence, $\overline{II}_b = 1$ (Fig. 6). In the feasibility test sections, we will demonstrate how this new convolved II is effectively used to incorporate additional material models related to smart bar computational material models. This supports the expandability of the proposed approach to include many new material models by devising a new material-specific new II. As long as the II conveys physical meaning and a manageable range of [0, 1], researchers can propose their own II for further complex material models.

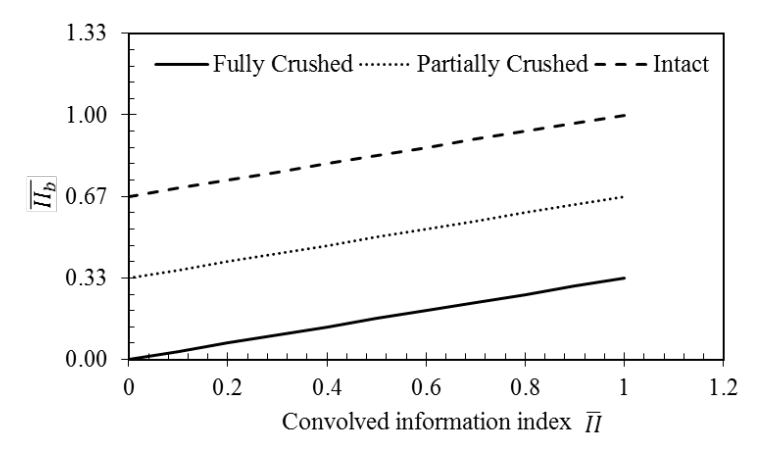


Fig. 6. The proposed mapping from the convolved information index \overline{II} to \overline{II}_h .

4. Flexible link function

4.1. Cubic regression spline-based link function

Another key enabler of the glass-box computational materials framework is the transparent and expressive LF, denoted as $\mathcal{L}_M(\overline{\Pi};\mathbf{a}) \to \mathbf{c}$, where \mathbf{a} is a set of free parameters of LF, and \mathbf{c} is a set of material coefficients for a given material M. LF seeks to offer a mathematical expression between $\overline{\Pi}$ and M, while evolutionary ML focuses on the evolution of \mathbf{a} of LF. In general, to aim the continuous evolution, LF can look to the flexible expressions of the free material coefficients instead of fixed values such as weights of hidden neurons of deep learning. Also, LF can provide an acceptable explanation of the relation between the physical rules and information in which the relationship is self-evolving with the increasing of data.

In this paper, GA is adopted as the main evolutionary algorithm. The choice of GA is sufficient to explain the feasibility of the self-evolving capability of LF's. The fitness scores of all organisms are recorded to obtain the prior best LF's in which the organism can represent each candidate for \mathbf{a} 's of LF's. There are two requirements of \mathcal{L}_M are: (1) The evolutionary algorithm should be integrated with the LF for consistent evolution with more experimental data, and (2) the LF should ultimately span the input-output spaces. As long as satisfying these two requirements, LF can be

selected from any activation functions, including popular functions in the ML community (Fig. 7 and Table 1). Our goal is to derive a flexible and transparent expression of a hidden relation between convolved II and computational material's coefficients **c**. Thus, this paper suggests a highly flexible CRS-based LF.

Table 1. Popular activation functions in ML methods.

Types	Definition	Range
Sigmoid	$f(x) = \frac{1}{1 + e^{-x}}$	(0,1)
Hyperbolic tangent (tanh)	$f(x) = \frac{(e^x - e^{-x})}{(e^x + e^{-x})}$	(-1,1)
Rectified Linear Unit (ReLU)	f(x)=0	for $x \le 0$
	f(x) = x	for $x > 0$

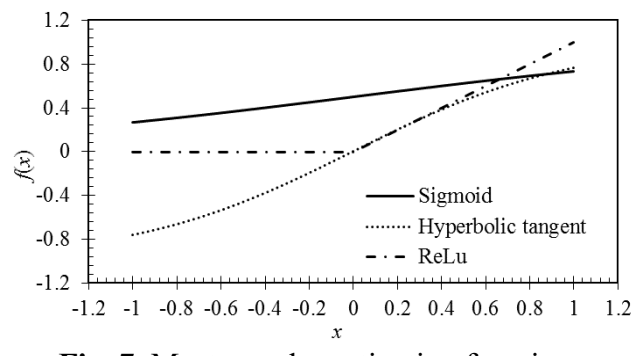


Fig. 7. Most popular activation functions.

CRS-based LF harnesses the flexibility of the connected cubic smooth functions (Hastie and Tibshirani [27]; Wood [28]). Briefly, it is instructive to touch upon the definition of CRS. It should be noted that this paper does not use CRS for regression-purpose. Rather, CRS is solely used for identifying hidden expressions of the material coefficients. The representation of smooth functions of CRS is given by

$$g(\mu_i) = f_1(x_{1i}) + f_2(x_{2i}) + \cdots$$
 (14)

where g is a smooth LF; $\mu_i \equiv \mathbb{E}(Y_i|x_i)$; Y_i is a response variable; x_{ji} is the jth covariate in a multidimensional vector \mathbf{x}_i where i indicates the ith instance; f_j is a smooth function corresponding to the jth covariate. After scaling, we can always make x_i lie in the interval [0, 1], and the smooth function f can be assumed to consist of q basis functions as

356
$$f(x) = \sum_{i=1}^{q} a_i b_i(x)$$
 (15)

where a_i is the unknown free parameter of the basis function; $b_i(x)$ is the *i*th basis function in which can be given as $b_1(x) = 1$, $b_2(x) = x$, and $b_{i+2} = R(x, z_i)$ for i = 1, ..., q-2; R(x, z) can be defined in a general form as

$$R(x,z) = \frac{\left[\left(z - \frac{1}{2}\right)^2 - \frac{1}{12}\right]\left[\left(x - \frac{1}{2}\right)^2 - \frac{1}{12}\right]}{4} - \frac{\left[\left(|x - z| - \frac{1}{2}\right)^4 - \frac{1}{2}\left(|x - z| - \frac{1}{2}\right)^2 + \frac{7}{240}\right]}{24}$$
(16)

where z is the knot location (i.e., point where the cubic curves are connected). Thus, the final smooth curve is made up of sections of cubic polynomial joined together so that they are continuous up to the 2^{nd} derivative at each knot, as illustrated in Fig. 8.

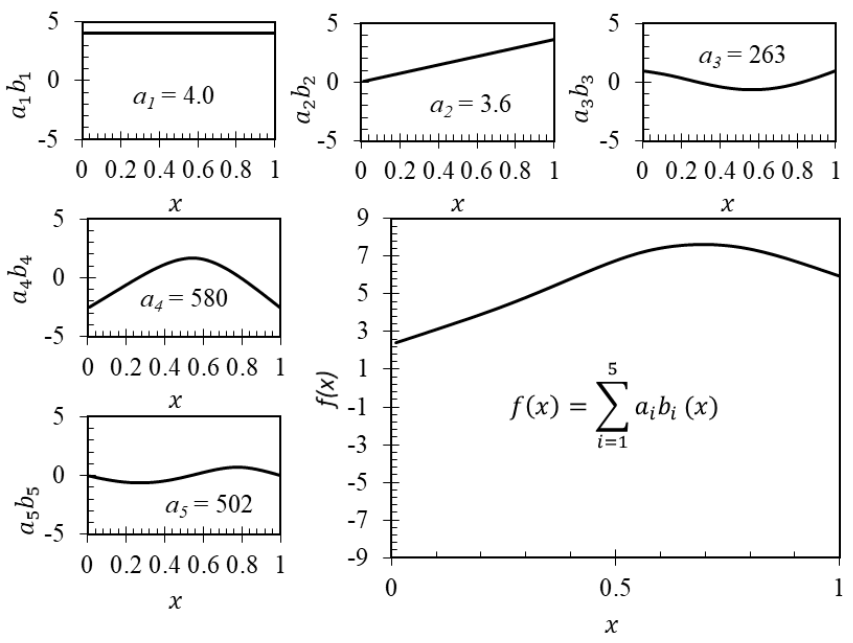


Fig. 8. Illustration of CRS with the decomposed five bases and the final weighted summation of the smooth function f(x) at the right bottom. Each box shows the free parameter a_i of each basis $b_i(x)$.

Inheriting the flexibility of the CRS bases, this paper proposes CRS-based LF of the convolved II (denoted as \overline{II}) as

$$\mathcal{L}_{M}(\overline{II}; \mathbf{a}) = a_{1}b_{1}(\overline{II}) + a_{2}b_{2}(\overline{II}) + \sum_{i} a_{i+2}b_{i+2}(\overline{II})$$
(17)

It should be noted that if a material behavior is known as simple (e.g., monotonic increasing or decreasing; Fig. 9), a simple form LF such as two-parameter exponential LF (Cho [26]) may suffice. Although exponential LF takes only two free parameters, Fig. 9 underpins its wide coverage in shapes and amplitudes. The two-parameter exponential LF is given as

377
$$\mathcal{L}_{M}(\overline{II}; \mathbf{a}) \equiv \exp[a_{1}(\overline{II})^{a_{2}}]$$
 (18)

Both CRS-based LF and exponential LF have excellent flexibility compared to the fixed activation functions (Fig. 7). Therefore, this paper advocates the highly flexible CRS-based LF and uses the exponential LF as a comparative study.

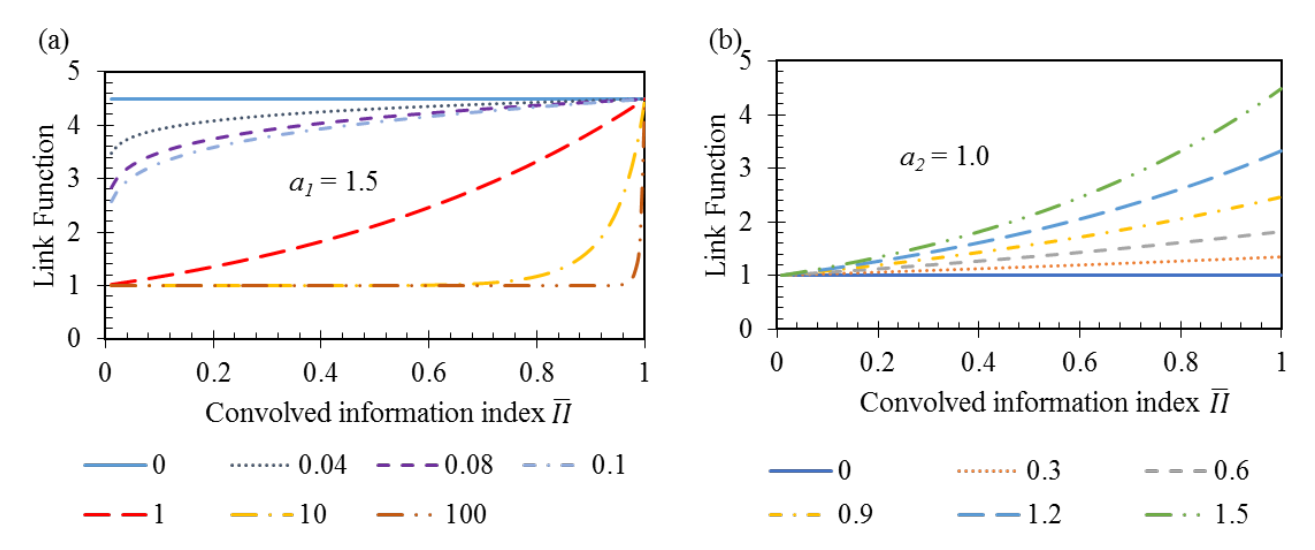


Fig. 9. Exponential LF: (a) convex and concave shapes controlled by a_2 ; (b) amplitude controlled by a_1 .

4.2. Remarks on pre-shrinking of the search range

If HFCS is light in terms of computational time, the evolutionary algorithm will successfully find the global optimum via typical fitness-based evolution, inheritance, spawning, and mutation processes. However, our paper deals with multi-scale computational material models required to analyze large-scale, highly nonlinear composite structures at their ultimate nonlinear behaviors (Cho [26]; Cho [38]). Using hundreds of CPUs, each HFCS may take hours to days, even with the aid of parallel computing (Cho and Porter [39]; Cho and Hall [40]). Therefore, it is practically important to shrink the vast search range in view of domain-specific knowledge. To offer a practical recommendation, in this section, we expound upon two cases: the desired maximum value of CRS-based LF (\mathcal{L}_M) occurs at the right end (i.e., the monotonic increasing case (Fig. 10a)), and the maximum happens in the middle of the span (i.e., the convex case (Fig. 10b)). It should be noted that this remedy shall be extended to cover different scenarios, but the bottom line will be similar. Also, if researchers can access sufficiently large computing resources, they may directly tackle the vast searching space without this recommendation.

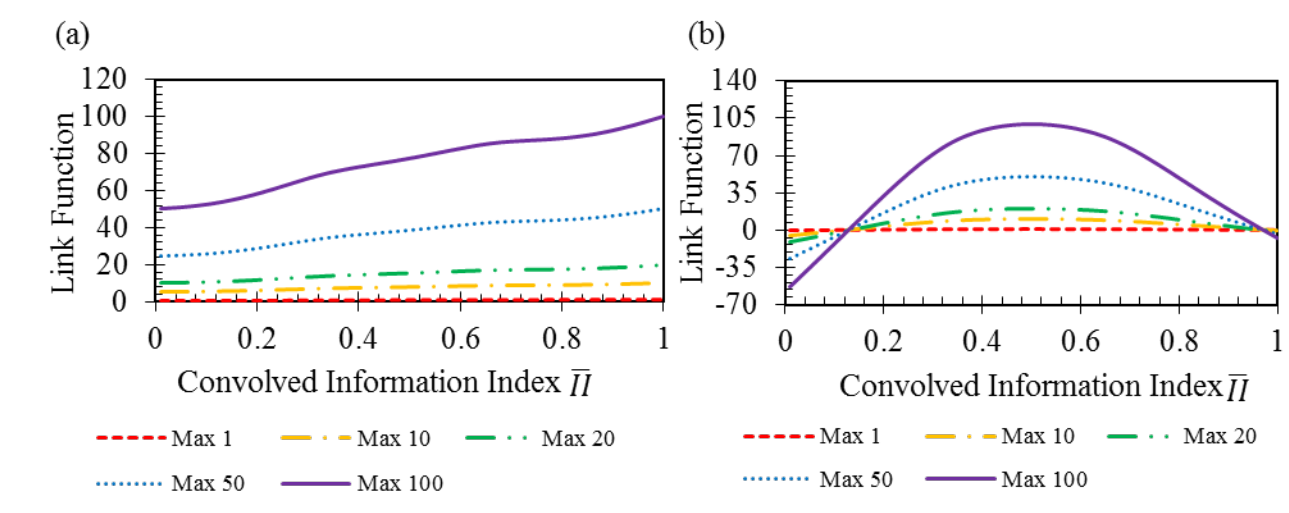


Fig. 10. The CRS-based LF's general shape for the desired maximum value: (a) monotonic increasing; (b) target maximum in the middle.

In the monotonic increasing case, the range of the free parameters of \mathcal{L}_M can be obtained by applying the general mathematical condition to find the maximum of a linear function.

$$\left. \frac{d\mathcal{L}_{M}}{dx} \right|_{x_{max}=1.0} \ge 0 \Rightarrow a_{2} + a_{3} \acute{b_{3}}(x_{max}) + a_{4} \acute{b_{4}}(x_{max}) + a_{5} \acute{b_{5}}(x_{max}) \ge 0 \tag{19}$$

where $\acute{b}_{\iota}(x_{max})$ is the first derivative of the basis functions that can be calculated, as shown in Fig. 11b. However, the conditions are slightly changed in the convex case while the range of the free parameters of \mathcal{L}_{M} can be obtained by applying the first and second derivatives to find the local maximum where the slope is zero. The detailed algebraic proofs are presented in Appendix D and E.

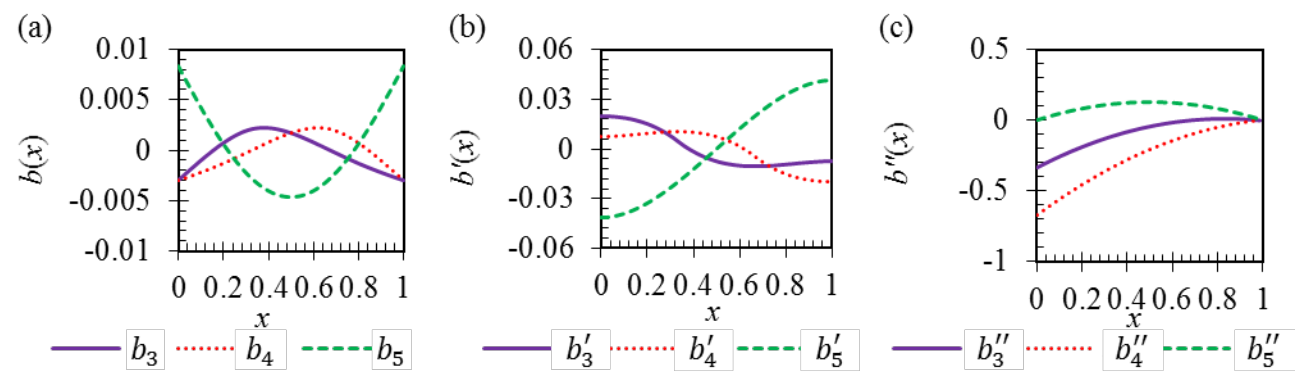


Fig. 11. The mathematical relation of the basis function: (a) three basis functions b_3 , b_4 , and b_5 ; (b) the first derivative of the basis functions; (c) the second derivative of the basis functions.

In general, Table 2 and Table 3 provide some recommendations to obtain the free parameters of \mathcal{L}_M for a different maximum target. It should be noted that these recommendations are not a strict limit of the search range. Instead, they may be used with discretion to find a meaningful relationship with substantially time-consuming simulations swiftly.

Table 2. Recommendations to follow monotonic increasing relation.

Target			CRS			Expor	nential
max of LF	a_1	a_2	аз	a_4	<i>a</i> 5	a_1	a ₂
1	[0.5, 1]	[0, 0.5]	[-168, 168]	[-168, 168]	[-120, 120]	0	[0, 100]
2	[1, 2]	[0, 1]	[-336, 336]	[-336, 336]	[-240, 240]	[0, 0.69]	[0, 100]
3	[1.5, 3]	[0, 1.5]	[-504, 504]	[-504, 504]	[-360, 360]	[0, 1.1]	[0, 100]
4	[2, 4]	[0, 2]	[-672, 672]	[-672, 672]	[-480, 480]	[0, 1.38]	[0, 100]
5	[2.5, 5]	[0, 2.5]	[-840, 840]	[-840, 840]	[-600, 600]	[0, 1.61]	[0, 100]
7.5	[3.5, 7.5]	[0, 3.5]	[-1176, 1176]	[-1176, 1176]	[-900, 900]	[0, 2.01]	[0, 100]
10	[5, 10]	[0, 5]	[-1680, 1680]	[-1680, 1680]	[-1200, 1200]	[0, 2.3]	[0, 100]
20	[10, 20]	[0, 10]	[-3359, 3359]	[-3359, 3359]	[-2400, 2400]	[0, 3]	[0, 100]
50	[25, 50]	[0, 25]	[-8398, 8398]	[-8398, 8398]	[-6000, 6000]	[0, 3.91]	[0, 100]
100	[50, 100]	[0, 50]	[-16800, 16800]	[-16800, 16800]	[-12000, 12000]	[0, 4.61]	[0, 100]

Table 3. Recommendations to have the maximum at the middle.

Target			CRS		
max of LF	a_1	a_2	a_3	<i>a</i> ₄	<i>a</i> ₅
1	[0.25, 1]	[0, 0.5]	[0, 320]	[0, 255]	[0, 107]
2	[0.5, 2]	[0, 1]	[0, 640]	[0, 511]	[0, 213]
3	[0.75, 3]	[0, 1.5]	[0, 960]	[0, 766]	[0, 320]

4	[1, 4]	[0, 2]	[0, 1280]	[0, 1022]	[0, 427]
5	[1.25, 5]	[0, 2.5]	[0, 1600]	[0, 1277]	[0, 533]
7.5	[1.88, 7.5]	[0, 3.5]	[0, 2400]	[0, 1916]	[0, 800]
10	[2.5, 10]	[0, 5]	[0, 3201]	[0, 2554]	[0, 1067]
20	[5, 20]	[0, 10]	[0, 6401]	[0, 5109]	[0, 2133]
50	[12.5, 50]	[0, 25]	[0, 16003]	[0, 12772]	[0, 5333]
100	[25, 100]	[0, 50]	[0, 32006]	[0, 25543]	[0, 10667]

5. Existing computational material models to be evolved by glass-box framework

One of the glass-box framework's novelties is that it can honor and leverage the existing material models in lieu of completely replacing them. Computational material models often have unknown material coefficients, which have critical roles in the material mechanisms. They are difficult to obtain from empirical calibrations because of complex heterogeneity and diverse BC's of real materials. Hence, this section describes how to use the proposed glass-box framework to dissolve the hidden relationship between the convolved II and the decisive, unknown material coefficients. It should be noted that the inclusion of other advanced material models is straightforward, and this paper focuses on how to expand them.

5.1. Glass-box framework for nonlinear quasi-brittle materials models

The first material mechanism is the fixed-type smeared crack model. The adopted crack model permits three orthogonal crack surfaces (Fig. 12b). The microscopic crack stress tensor σ^{cr} can be determined by crack-normal stress function Ψ_n and crack-tangential stress function Ψ_s . In particular, this paper adopts quasi-brittle material models (Thorenfeldt [41]; Taucer et al. [42]; Reinhardt [43]) for updating microscopic stresses on the three crack surfaces. The mesh objectivity about tensile crack can be achieved by adopting the crack bandwidth (Bazant and Oh [44]; Cho [45]).

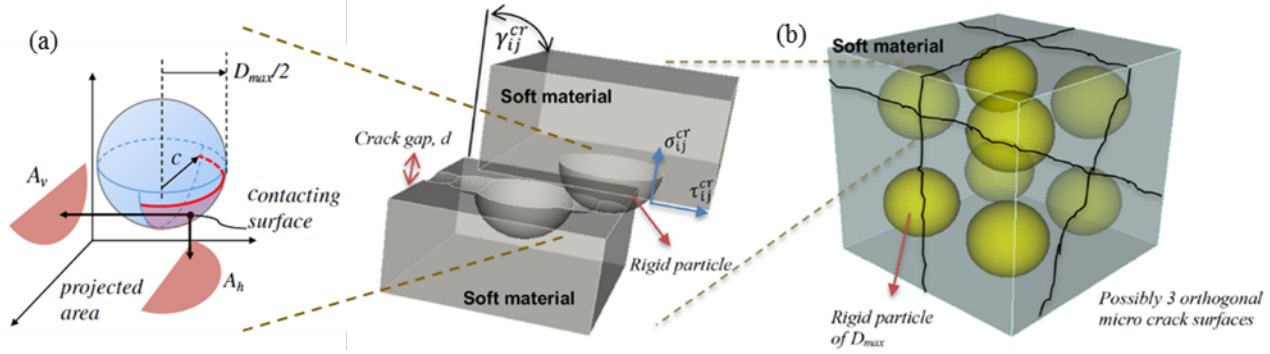


Fig. 12. Microphysical mechanisms of the quasi-brittle materials used for feasibility tests: (a) 3D nonlinear shear mechanism-based soft matrix-rigid hemisphere interlocking (adapted from Cho [38], Cho [45]); (b) Multi-directional smeared crack mechanism allowing three orthogonal cracks over random-sized aggregates (adapted from Cho [26]).

In term of tangential stress function Ψ_s , Cho [38] had derived a three-dimensional (3D) interlocking model for describing the degradation of tangent shear resistance at the cracked material by using the tribology and the 2-D interlocking model (Fig. 12a). Tribology assumes that the plastic deformation occurs on the hemisphere part because of the simple contact with a rigid flat plate (Jackson and Green [46]). The present work is assuming that the permanent plastic deformation happens at the soft matrix part only. The tangent shear stiffness G can be obtained by

$$G(\tilde{\varepsilon}) = C_{cs} \frac{G_0}{(1+\mu)} \frac{2}{\pi} \left\{ \tan^{-1} \sqrt{\tilde{\varepsilon}^{-2} - 1} - \tilde{\varepsilon} \sqrt{1 - \tilde{\varepsilon}^2} + \frac{\pi}{2} \mu (1 - \tilde{\varepsilon}^2) \right\}$$
 (20)

where C_{cs} is the ambient condition-dependent empirical coefficient; G_0 is the elastic shear modulus; μ is the friction coefficient; $\tilde{\varepsilon} = 2d/D_{max}$. The relationship between $\tilde{\varepsilon}$ and ε in one-dimensional case given by $\varepsilon = \tilde{\varepsilon}(D_{max}/2)/L$, where ε is the normal strain to the crack surfaces; d is the distance between crack surfaces; L is the length of the element; D_{max} is the diameter of the ideal particle. The physical explanation of the interaction between the rigid particle and soft matrix offers a clear understanding of the realistic behavior of cyclic shear resistance.

Next, normal stress function Ψ_n can be obtained by the following

$$\Psi_{n}(\varepsilon_{i}^{cr}) = \begin{bmatrix}
\varepsilon_{i}^{cr} < 0 & \sigma_{i}^{cr} = -(\beta \cdot \sigma_{c})\zeta \left(\frac{n}{n-1+\zeta^{n \cdot k}}\right) \\
(f_{t}/\varepsilon_{t})\varepsilon_{i}^{cr} & 0 < \varepsilon_{i}^{cr} \le \varepsilon_{t} \\
f_{t}\left[1 - \left\{\frac{\varepsilon_{i}^{cr} - \varepsilon_{i}}{\varepsilon_{u} - \varepsilon_{t}}\right\}^{c}\right] & \varepsilon_{t} < \varepsilon_{i}^{cr} \le \varepsilon_{u} \\
0 & \varepsilon_{u} < \varepsilon_{i}^{cr}
\end{cases} \tag{21}$$

where σ_i^{cr} [MPa] is the current normal stress on the *i*th crack surface; β is the ambient condition-dependent strength enhancement factor; σ_c [MPa] is the compressive strength without lateral constraints; $\zeta = \varepsilon_i^{cr}/\varepsilon_0$; ε_i^{cr} is the normal strain on the *i*th crack surface; ε_0 is the strain at the compressive strength; $n = 0.8 + \beta \cdot \sigma_c/17$; the parameter k = 1 for $\varepsilon_0 < \varepsilon_i^{cr} < 0$, or $k = 0.67 + \beta \cdot \sigma_c/62$ for $\varepsilon_i^{cr} < \varepsilon_0$. β , C_{cs} , and μ are the unknown material coefficients, which have critical roles in the material mechanisms, as shown in Fig. 13. They are difficult to obtain from empirical calibrations because of the irregular asperity of cracked surfaces and the heterogeneity of real materials. Hence, this paper uses the proposed framework to dissolve the relationship between (β, C_{cs}, μ) and II.

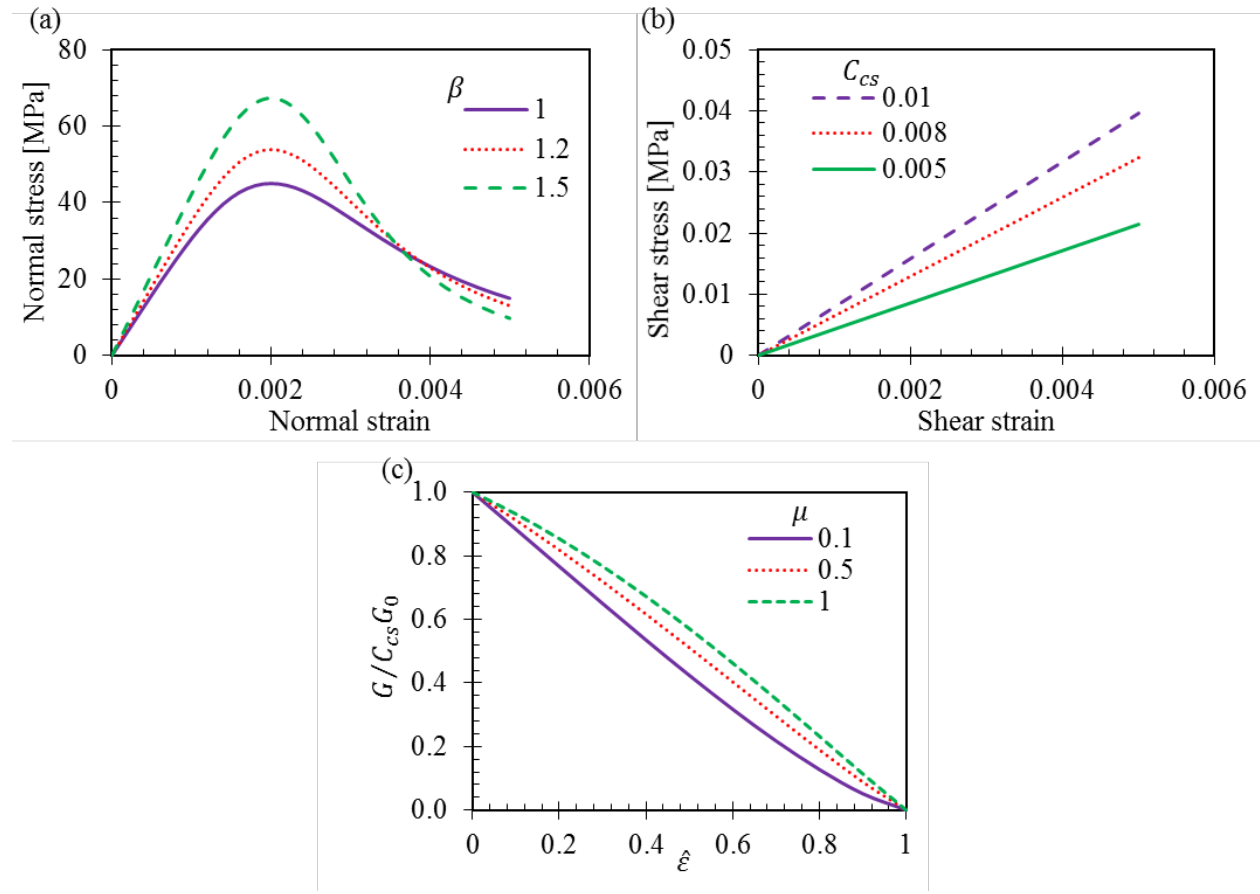


Fig. 13. The critical role of β , C_{cs} , and μ in the mechanisms: (a) the impact of different $\beta's$ on the normal stress; (b) the impact of different $C_{cs}'s$ on the shear stress; (c) the impact of different μ 's on the tangent shear stiffness G.

5.2. Glass-box framework for a smart bar model with progressive buckling

This section describes how the glass-box framework can be used to learn the hidden decisive material coefficient of the smart bar model, which can capture progressive buckling. The target smart bar model is a generalized Menegotto-Pinto bar model capable of capturing progressive bar buckling, yielding, and rapture in a smooth transition during reversed loading. The model is denoted as "smart" since it leverages the topological information and surrounding quasi-brittle materials' damage information as briefly described in Section 3. However, the smart bar model has a hidden decisive material coefficient. To derive the material coefficient, many used idealized experiments or analytical formulation (e.g., Dhakal and Maekawa [37]). Although a deep reality-

laboratory gap remains, the general knowledge gleaned from the previous studies is meaningful. In sum, researchers found: (1) the average compressive stress is smaller than the point wise stress after the onset of buckling; (2) the average post-buckling compressive stress becomes constant after it decreases to the post-buckling residual compressive strength c_1f_y where c_1 is the factor for residual strength after buckling and f_y is yielding stress; (3) the degradation rate of average compressive stress is almost constant, and it can be expressed by the post-buckling negative stiffness of the bar c_2E_s as

498
$$\sigma = \sigma^* - c_2 E_s(\varepsilon - \varepsilon^*); \text{ for } \varepsilon > \varepsilon^*$$
 (22)

where σ^* is the stress at the onset of buckling. E_s is Young's modulus of the reinforcing bar; ε is current strain; ε^* is the strain at the onset of buckling, and it can be defined as

501
$$\frac{\varepsilon^*}{\varepsilon_y} = \kappa \left(55 - 2.3 \sqrt{\frac{f_y}{100}} \frac{L_b}{D_s} \right); \quad \text{otherwise } \varepsilon^* \ge 7\varepsilon_y$$
 (23)

where ε_y is the strain at yielding; f_y is stress at yielding. D_s is the diameter of the bar cross-section.

 L_b is the updated buckling length defined by Cho [38] as

$$L_b \equiv \sum_{L_0^{(i)} for \ \forall e_i^1 \in BU_m} k L_0^{(i)}$$
 (24)

where $L_0^{(i)}$ is initial buckling length of the *i*th steel bar (denoted by e_i^1 meaning a line entity); BU_m is the basic topological group consisting of a bar and its adjacent solid elements; k is the effective length factor.

Herein, κ , c_1 , and c_2 are the unknown material coefficients, which are difficult to obtain from the empirical calibrations because the reinforcing system deforms in a complicated way and depends on different factors related to microstates of surrounding materials and diverse BC's. Therefore,

this paper employs the proposed glass-box framework to unravel the relationship between (κ, c_1, c_2) and \overline{II}_b (Fig. 14).

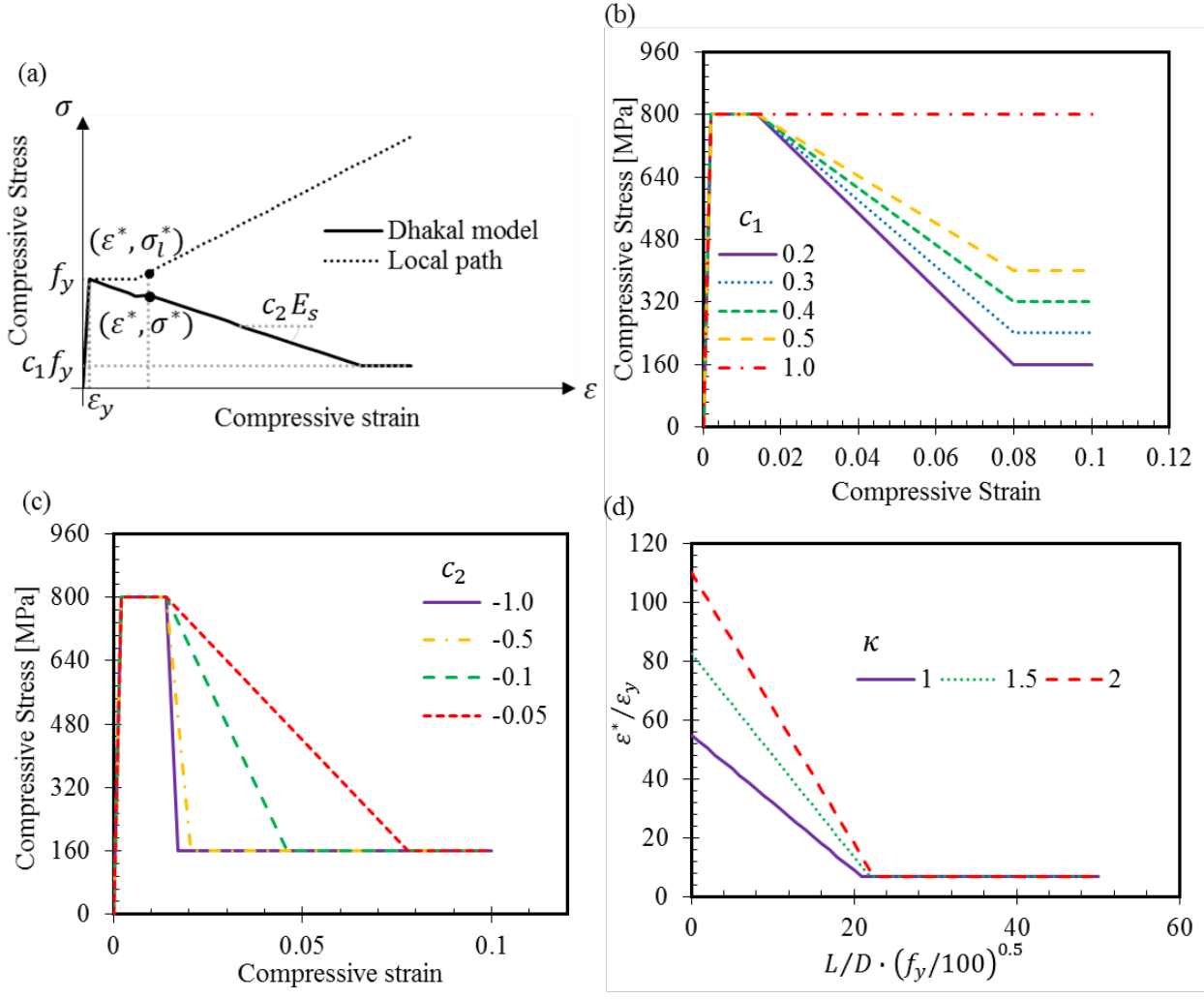


Fig. 14. Coefficient effects on the stress-strain curve: (a) buckling model proposed by (Dhakal and Maekawa [37]) where σ_l^* is point wise stress corresponding to ε^* (strain at the onset of buckling); (b) using different factors for residual strength after buckling c_1 ; (c) using different reduction factors for post-buckling (softening regime) c_2 ; (d) the effect of different κ on the onset of buckling strain ε^* .

5.3. Rationales for the selected material mechanisms

We briefly explain why this study selected the aforementioned four microphysical mechanisms. A rectangular wall (denoted WSH5 from Dazio et al. [48]) has been used to show the key aspect and the role of different mechanisms in nonlinear regimes (Fig. 15). First, the multi-directional, fixed-

type smeared crack model (denoted as "Adv. Concrete" in Fig. 15a) is adopted since it can preserve the actual crack directions allowing at most three orthogonal cracks. The preserved physical crack surfaces are important to incorporate nonlinear shear mechanism ("NL-shear" in Fig. 15a) since the NL-shear is based on the physical interaction between the rigid particle and soft matrix (Cho [38]). The importance of the Adv. Concrete and NL-shear in capturing nonlinear degradation of shear capacity is shown by the green-colored curve in Fig. 15a. Next, this study adopts the nonlinear reinforcing steel bar mechanism (denoted P-Buckling) based on the generalized Menegotto-Pinto hysteresis (Cho [38]). The bar mechanism can utilize the topological information of surrounding concrete's damage (e.g., partially intact or crushing) of the center bar capable of describing progressive compressive buckling of the bar. As shown in yellow and red curves in Fig. 15a, the inclusion of the P-buckling mechanism helps the curve approach to the real envelope (black line) at the large displacement ranges (far left and right regimes of Fig. 15a). It should be noted that there are ample rooms to incorporate other advanced mechanisms such as multiscale or plasticity theories in the future extention, but the adopted four mechanisms are sufficient to support the goal of this study.



541

542

543

525

526

527

528

529

530

531

532

533

534

535

536

537

538

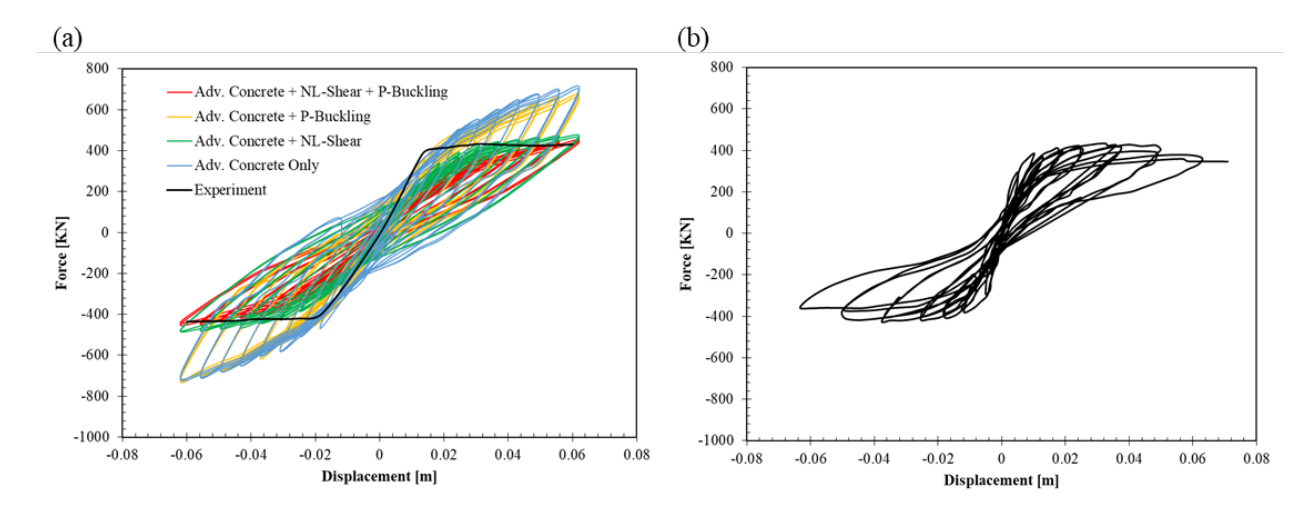


Fig. 15. Comparison among simulations with different nonlinear mechanisms: (a) "Adv Concrete" means multi-directional smeared crack mechanism. "NL-Shear" means the nonlinear shear

mechanism based on rigid particle-soft matrix interlocking. "P-Buckling" means the progressive buckling steel bar mechanism. The experiment line indicates the outer envelope of the real force-displacement curve of (b) (adapted from experiment of Dazio et al. [48]).

547548

546

544545

6. Feasibility Test

- Schmidt and Lipson [47] used externally observable physics rules to calculate the prediction errors.
- 550 Similarly, the proposed glass-box framework can leverage the externally observed global
- responses as a measure of error or prediction performance metric. Thus, raw fitness scores (i.e.,
- the inverse of error) are given by

$$R(\mathbf{a}) = \frac{1}{2} \left(\left| \max_{\forall t} \mathbf{F}_r - \max_{\forall t} \mathbf{F}_p \right| + \left| \min_{\forall t} \mathbf{F}_r - \min_{\forall t} \mathbf{F}_p \right| \right)$$
 (25)

- where \mathbf{F}_r and \mathbf{F}_p are the nonlinear force responses from real experiment and simulation prediction,
- respectively. The adjusted fitness scores \mathcal{F}_a are calculated by

$$\mathcal{F}_a = \frac{1}{\left(1 + R(\mathbf{a})\right)} \tag{26}$$

Lastly, the normalized fitness scores \mathcal{F} can be calculated by

$$\mathcal{F} = \frac{\mathcal{F}_a}{\sum_{b \neq s} \mathcal{F}_a} \tag{27}$$

- The uncertainty behind the GA-driven LF's and subsequent computational predictions can be
- carried by the standard deviation of absolute values of relative errors of all organisms in the best
- so far generation, which termed as σ_{Er}

$$\sigma_{Er} = \sqrt{Var(|Err|)} = \sqrt{n_s^{-1} \sum_{\forall s} |\Gamma(s)|^2 - \left(n_s^{-1} \sum_{\forall s} |\Gamma(s)|\right)^2}$$
 (28)

563 where

$$\Gamma(s) = \frac{1}{2} \left(\frac{\left| \max_{\forall t} \mathbf{F}_r - \max_{\forall t} \mathbf{F}_p \right|}{\left| \max_{\forall t} \mathbf{F}_r \right|} + \frac{\left| \min_{\forall t} \mathbf{F}_r - \min_{\forall t} \mathbf{F}_p \right|}{\left| \min_{\forall t} \mathbf{F}_r \right|} \right)$$
(29)

where s and n_s are an organism and the total organisms in the generation, respectively.

6.2. Diverse large-scale specimens for feasibility test

Table 4, Fig. 16, and Fig. 17 summarize material properties, geometric, and reinforcement information of various walls used to train the glass-box framework. The five rectangular walls (named WSH 1-5) were experimented by Dazio et al. [48]. The U-shaped wall (named TUB) was investigated by Beyer et al. [49].

Table 4. Material properties of specimen walls.

Description	WSH1	WSH2	WSH3	WSH4	WSH5	TUB
Width (mm)	2000	2000	2000	2000	2000	1300
Length (mm)	150	150	150	150	150	1050
Height (mm)	4560	4560	4560	4560	4560	3350
Axial load (KN)	689	691	686	695	1474	780
Compressive strength (MPa)	45	45	45	45	45	55
Module of elasticity (MPa)	31529	31529	31529	31529	31529	34856
Strain at compressive strength	0.002	0.002	0.002	0.002	0.002	0.002
Tensile strength (MPa)	4.5	4.5	4.5	4.5	4.5	5.5
Strain at tensile	0.000143	0.000143	0.000143	0.000143	0.000143	0.000158
	D3.5(656)	D4.2(526)	D4.2(562)	D6(519)	D4.2(562)	D6(518)
D (Diameter in mm)	D6(590)	D6(515)	D6(489)	D8(650)	D6(550)	D12(471)
Yielding stress (MPa)	D10(600)	D10(671)	D8(680)	D12(600)	D8(700)	
			D12(700)			
	D3.5(662)	D4.2(583)	D4.2(615)	D6(559)	D4.2(615)	D6(681)
D (Diameter in mm)	D6(600)	D6(535)	D6(552)	D8(714)	D6(559)	D12(574)
Ultimate stress (MPa)	D10(620)	D10(747)	D8(700)	D12(675)	D8(714)	
			D12(726)			



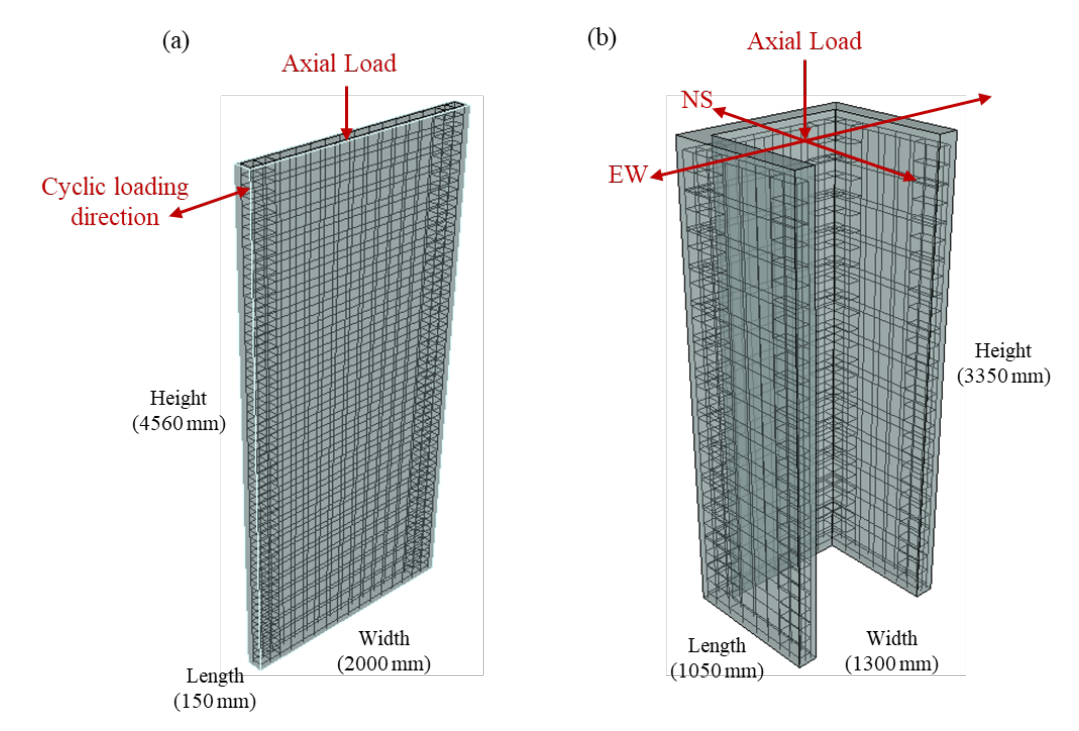


Fig. 16. Plan view for rectangular and U-shaped wall: (a) Rectangular wall named as WSH 1~5; (b) U-shaped wall named as TUB. Black lines are actual reinforceing steel bars' layouts which are all modeled in the full-scale computational simulation with space truss elements.

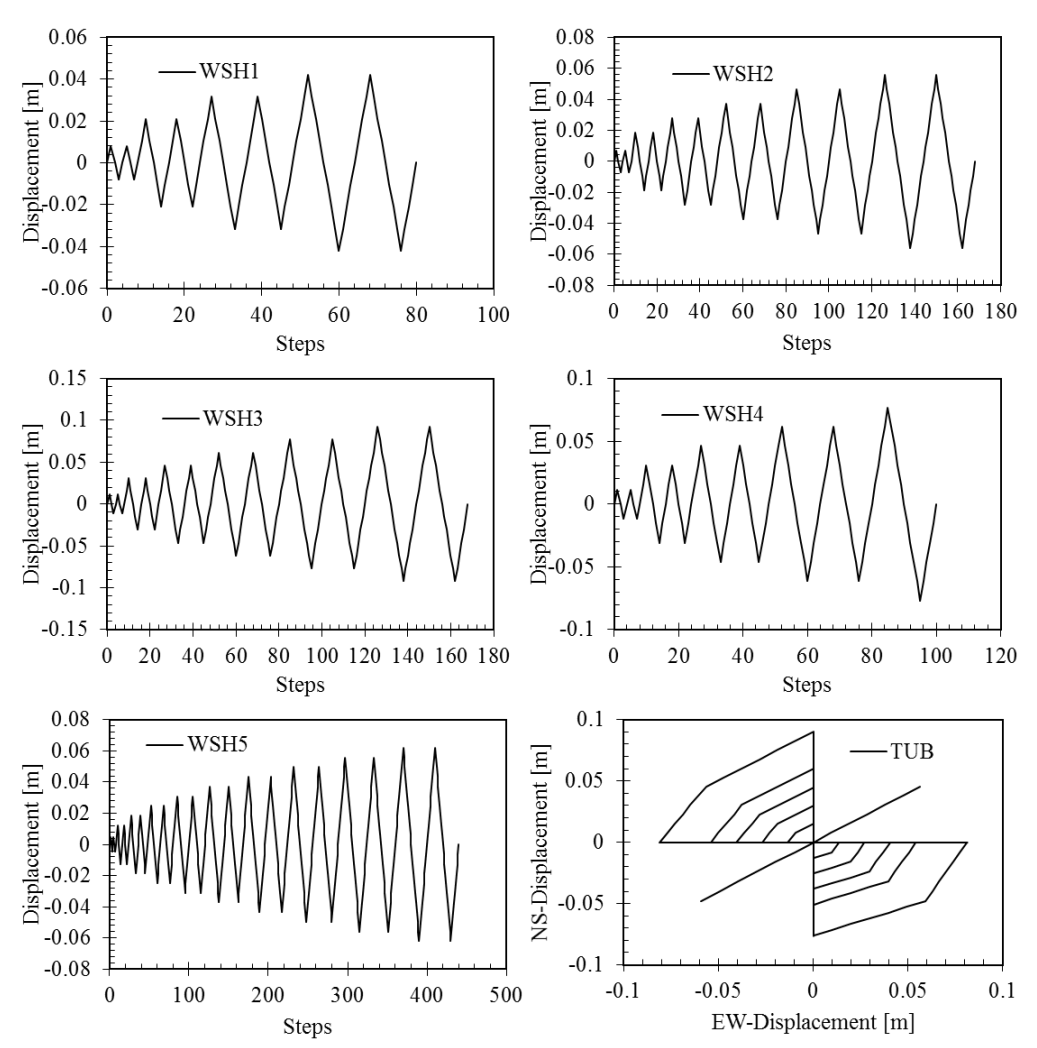


Fig. 17. Displacement history for each wall.

6.3. Set-up of evolutionary algorithm and initial material coefficients

The main settings for GA are as follows. The mutation rate is fixed to be 0.02 to control the random "jump" in the location of the generated solution. Four genes and four alleles encode the real variable. The LF parameter ranges are set based on each material coefficient range. For example, $\mu = 0.4$ has been well-proven by Walraven [50], so the range is set to be [0,1] to search for enough range. $c_1 = 0.2$ is the minimum value based on experimental results of a single bar without surrounding concrete recommended by Dhakal and Maekawa [37], while $c_1 = 1.0$ is the maximum possible residual strength, which is the same as the yield strength of steel, so the range is set to be

[0,1]. Moreover, $c_2 = -0.02$ is the minimum degradation rate recommended by Dhakal and Maekawa [37], which is reasonable on a single bar without any surrounding concrete, but the range of c_2 is set to be [-0.02,0], where $c_2 = -0.005$ shows a large enough ultimate strain of steel bar. In addition, $\kappa = 1.0$ is the minimum value recommended by (Dhakal and Maekawa [37]) to predict the onset of buckling on a single bar without surrounding concrete, while $\kappa = 2.0$ is the maximum possible value that can delay the onset of buckling since the bar steel is surrounded by concrete, so the range is set to be [0,2]. However, the range of β is set to be [0,12] to search for enough range where default $\beta = 1.0$. Also, the range for scaling of C_{cs} (denoted as S_c) is set to be [0,4300] where the default of S_c is equal to one. It should be noted here that $C_{cs} = S_c \times 0.0001$, so the range of C_{cs} can be [0,0.43] based on Cho [26]. Moreover, in order to compare between exponential and CRS-based LF's for the paper in the following sections, the range of α is set to be [0, 1] and [0, 4.5] which α is an enhancement factor for ε_0 . Table 5 and Table 6 show the LF parameter ranges for each material coefficient that has been used in this work. In addition, two models (called Model I and Model II) were used in the feasibility test. Model I, which is adopted from Cho [26], and has only two physical targets (β , and C_{cs}), has been used in this work to validate and compare between CRS-based and exponential LF (Eq. 30). Model II, which is proposed in this work, has been used to add more physical targets such as $(\mu,\,c_1,\,c_2,\,\kappa)$ to learn and provide the mathematical expressions for these empirical coefficients, so it has been using 6-coefficients in this model (Eq. 30 and Eq. 31).

591

592

593

594

595

596

597

598

599

600

601

602

603

604

605

606

607

608

$$\begin{bmatrix} \beta(\overline{II}) = \mathcal{L}_{\beta}(\overline{II}; \mathbf{a}_{\beta}) \\ C_{cs}(\overline{II}) = \mathcal{L}_{S_{c}}(\overline{II}; \mathbf{a}_{S_{c}}) \times 0.0001 \end{bmatrix}$$
(30)

611
$$\begin{bmatrix}
\mu(\overline{II}) = \mathcal{L}_{\mu}(\overline{II}; \mathbf{a}_{\mu}) \\
\kappa(\overline{II}, \overline{II}_{b}, t) = \mathcal{L}_{\kappa}(\overline{II}, \overline{II}_{b}, t; \mathbf{a}_{\kappa}) \\
c_{1}(\overline{II}, \overline{II}_{b}, t) = \mathcal{L}_{c_{1}}(\overline{II}, \overline{II}_{b}, t; \mathbf{a}_{c_{1}}) \\
c_{2}(\overline{II}, \overline{II}_{b}, t) = \mathcal{L}_{c_{2}}(\overline{II}, \overline{II}_{b}, t; \mathbf{a}_{c_{2}})
\end{bmatrix}$$
(31)

where \mathcal{L}_{β} is the LF of beta; \mathbf{a}_{β} is a free parameter vector of \mathcal{L}_{β} to be determined by the evolutionary algorithm; t is the time step since \overline{II}_b is dependent on current damage.

It should be noted that β , C_{cs} , and μ are material coefficients that affect the strength of the brittle material; hence, convolved II has been used to unravel the hidden relationship between these material coefficients and II. However, κ , c_1 , and c_2 are material coefficients that affect the buckling of the reinforcement steel, in which it is dependent on the current damage of the surrounding material at the time step t and the adjacent information of the brittle material; hence, \overline{II}_b has been used for these material coefficients.

Table 5. The initial ranges for the LF free parameters of the new physical targets.

	CRS-based LF					
Parameters	$\mu \in [0,1]$	$c_1 \in [0,1]$	$c_2 \in [-0.2, 0]$	$\kappa \in [0, 2]$		
a_1	[0, 0.5]	[0, 0.5]	[-0.05, 0]	[0, 1]		
a_2	[0, 0.5]	[0, 0.5]	[-0.05, 0]	[0, 1]		
аз	[0, 288]	[0, 288]	[-29, 0]	[0, 576]		
a_4	[0, 288]	[0, 288]	[-29, 0]	[0, 576]		
as	[0, 120]	[0, 120]	[-12, 0]	[0, 240]		
<i>Z1</i>	[0, 0.333]					
<i>Z</i> 2	[0.333, 0.6667]					
<i>Z</i> 3	[0.6667, 1]					

Table 6. The setting used for feasibility tests.

	Exponential LF					
Parameters	$\alpha \in [0,1]$	$\alpha \in [0, 4.5]$	$\beta \in [0, 12]$	$S_c \in [0,4300]$		
a_1	[-100, 0]	[0, 1.5]	[0, 2.52]	[0, 8.39]		
a_2	[-1, 0]	[0, 10]	[0, 10]	[0, 10]		
	CRS-based LF					
a_1	[0, 1E-6]	[0, 2.25]	[0, 5]	[0, 10]		
a_2	[0, 1E-6]	[0, 2.25]	[0, 5]	[0, 2000]		
аз	[0, 1E-6]	[0, 756]	[0, 1000]	[0, 1E+6]		

a4	[0, 1E-6]	[0, 756]	[0, 1000]	[0, 1E+6]		
a_5	[0, 1E-6]	[0, 540]	[0, 1000]	[0, 1E+6]		
Z1	[0, 0.333]					
z_2	[0.333, 0.6667]					
<i>Z</i> 3	[0.6667, 1]					

626

7. Discussion on feasibility test results

7.1. Interpretation of the identified rules

- The main goal of the glass-box framework is to learn the hidden physical rules by providing
- mathematical expressions about the target material coefficients and the convolved II through LF.
- From the statistical angle, (Eq. 7) shows that each convolved II can be considered as marginal
- 630 likelihood with the Gaussian conditional probability $\mathcal{N}(\mathbf{x}_{(i)}, L^2)$:

631
$$\overline{II}(\mathbf{x}_{(i)}) = \mathbb{E}_{\mathcal{N}(\mathbf{x}_{(i)}, L^2)}(II) = \int_V \left(L\sqrt{2\pi}\right)^{-N} \exp\left(-\frac{|\mathbf{x}_{(i)} - \boldsymbol{\xi}|^2}{2L^2}\right) \left(II(\boldsymbol{\xi})\right) d\boldsymbol{\xi}$$
(32)

- where the dimension N = 3; the spatial influence range L = 0.001 m; $\mathbf{x}_{(i)} \in V$ is *i*th material point
- 633 (or integration point) in the domain V. An explicit form of the best-so-far LF can help to explain
- and show the hidden relationships. For instance, the identified physical rule about β and the II in
- a clear CRS form is given by

$$\beta(\mathbf{x}_{(i)}) = a_1 + a_2 \times \overline{II}(\mathbf{x}_{(i)}) + \sum_{j=1}^3 a_{j+2} \times b_{j+2} \overline{II}(\mathbf{x}_{(i)})$$

$$= a_1 + a_2 \times \mathbb{E}_{\mathcal{N}(\mathbf{x}_{(i)}, L^2)}(II) + \sum_{j=1}^3 a_{j+2} \times b_{j+2} \left(\mathbb{E}_{\mathcal{N}(\mathbf{x}_{(i)}, L^2)}(II)\right)$$
(33)

- where a is presented in Table 7, and plots of the above bases are shown in Fig. 18. Similarly,
- with different \mathbf{a} , the identified rule of C_{cs} and the convolved II is given by

639
$$C_{cs}(\mathbf{x}_{(i)}) = a_1 + a_2 \times \mathbb{E}_{\mathcal{N}(\mathbf{x}_{(i)}, L^2)}(II) + \sum_{i=1}^{3} a_{j+2} \times b_{j+2} \left(\mathbb{E}_{\mathcal{N}(\mathbf{x}_{(i)}, L^2)}(II) \right)$$
(34)

- where **a** is presented in Table 7, and plots of the above bases are shown in Fig. 19. These physical
- rules about β and C_{cs} are not fixed, nor unique. Instead, these rules propose the best-so-far,

approximate expressions regarding the target phenomena. Still, compared to the "black-box" style prediction of traditional ML methods, the identified rules are meant for future investigations using domain-knowledge.

In general, the feasibility test with micro-physical material models showed the capability of the framework in obtaining reasonable expressions for the role of material coefficients in the material mechanisms. By the flexibility and transparency of LF, the discovered physical rule may lead to

numerous possible rules.

Table 7. The best-so-far free parameters of CRS-based LF.

Table /.	1116 0631-30-1	ai nee parai	neters of Cr	CS-based L1	•
β	C_{cs}	μ	c_1	c_2	κ
4.00	0.00031	0.33	0.41	-0.02	0.4
3.61	0.027	0.22	0.2	-0.025	0.64
263	77.25	22.59	253	-20.36	368.19
580	70.59	214.69	45.18	-10.46	350.12
502	87.84	89.88	106.35	-11.06	74.35
0.12	0.31	0.15	0.2	0.28	0.08
0.56	0.58	0.43	0.45	0.6	0.36
0.78	0.71	0.91	0.9	0.94	0.98
	β 4.00 3.61 263 580 502 0.12 0.56	β C_{cs} 4.00 0.00031 3.61 0.027 263 77.25 580 70.59 502 87.84 0.12 0.31 0.56 0.58	β C_{cs} μ 4.00 0.00031 0.33 3.61 0.027 0.22 263 77.25 22.59 580 70.59 214.69 502 87.84 89.88 0.12 0.31 0.15 0.56 0.58 0.43	β C_{cs} μ c_1 4.00 0.00031 0.33 0.41 3.61 0.027 0.22 0.2 263 77.25 22.59 253 580 70.59 214.69 45.18 502 87.84 89.88 106.35 0.12 0.31 0.15 0.2 0.56 0.58 0.43 0.45	4.00 0.00031 0.33 0.41 -0.02 3.61 0.027 0.22 0.2 -0.025 263 77.25 22.59 253 -20.36 580 70.59 214.69 45.18 -10.46 502 87.84 89.88 106.35 -11.06 0.12 0.31 0.15 0.2 0.28 0.56 0.58 0.43 0.45 0.6

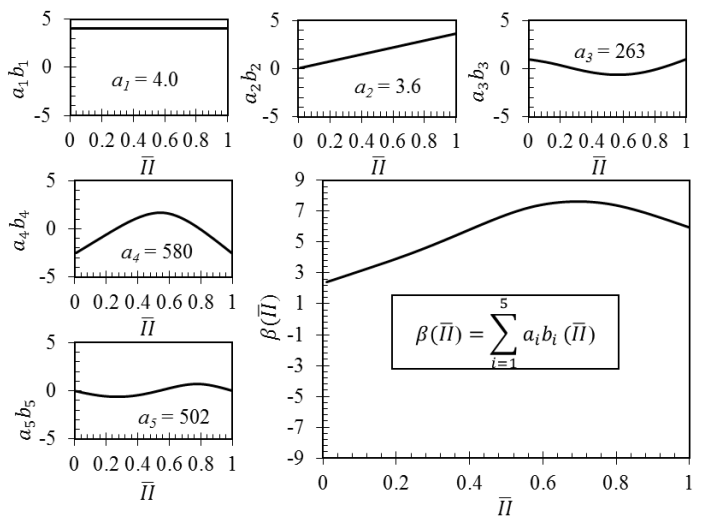


Fig. 18. The decomposed five bases and the final weighted summation of the smooth function $\beta(\overline{II})$ at the right bottom. Each box shows the parameter a_i of each basis $b_i(x)$.

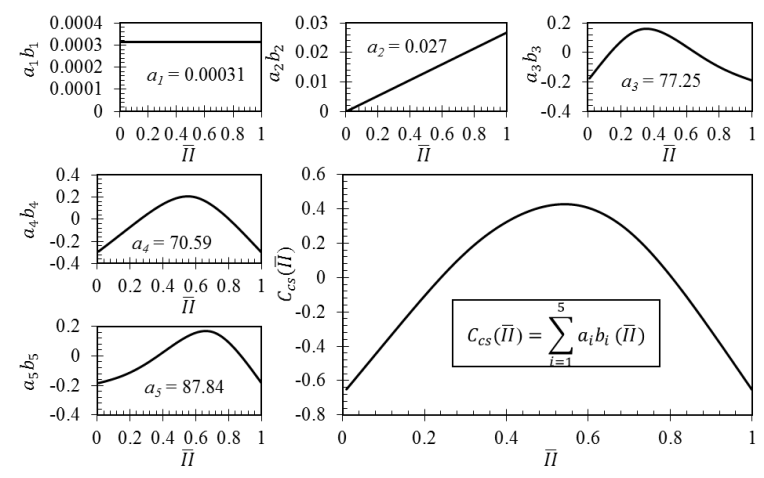


Fig. 19. The decomposed five bases and the final weighted summation of the smooth function $C_{cs}(\overline{II})$ at the right bottom. Each box shows the parameter a_i of each basis $b_i(x)$.

7.2. CRS-based LF's versus manually calibrated high-fidelity simulation

As shown in Fig. 20 and Table 8, the best-so-far result for each wall compares the prediction in terms of force and displacements using the glass-box framework and a parallel multi-scale finite element analysis (FEA) platform named VEEL (Cho [38]; Cho and Porter [39]). The training set starts with WSH 1, which has the least minimum error, and because of that, the prior best for WSH 1 is reserved for other walls. The glass-box framework with CRS-based LF shows less error than the default VEEL. Furthermore, as the GA learns the hidden relationship between \overline{II} and (β, C_{cs}) , the framework can provide a mathematical expression between the II and the coefficients through LF using a single target LF, as shown in Fig. 21.

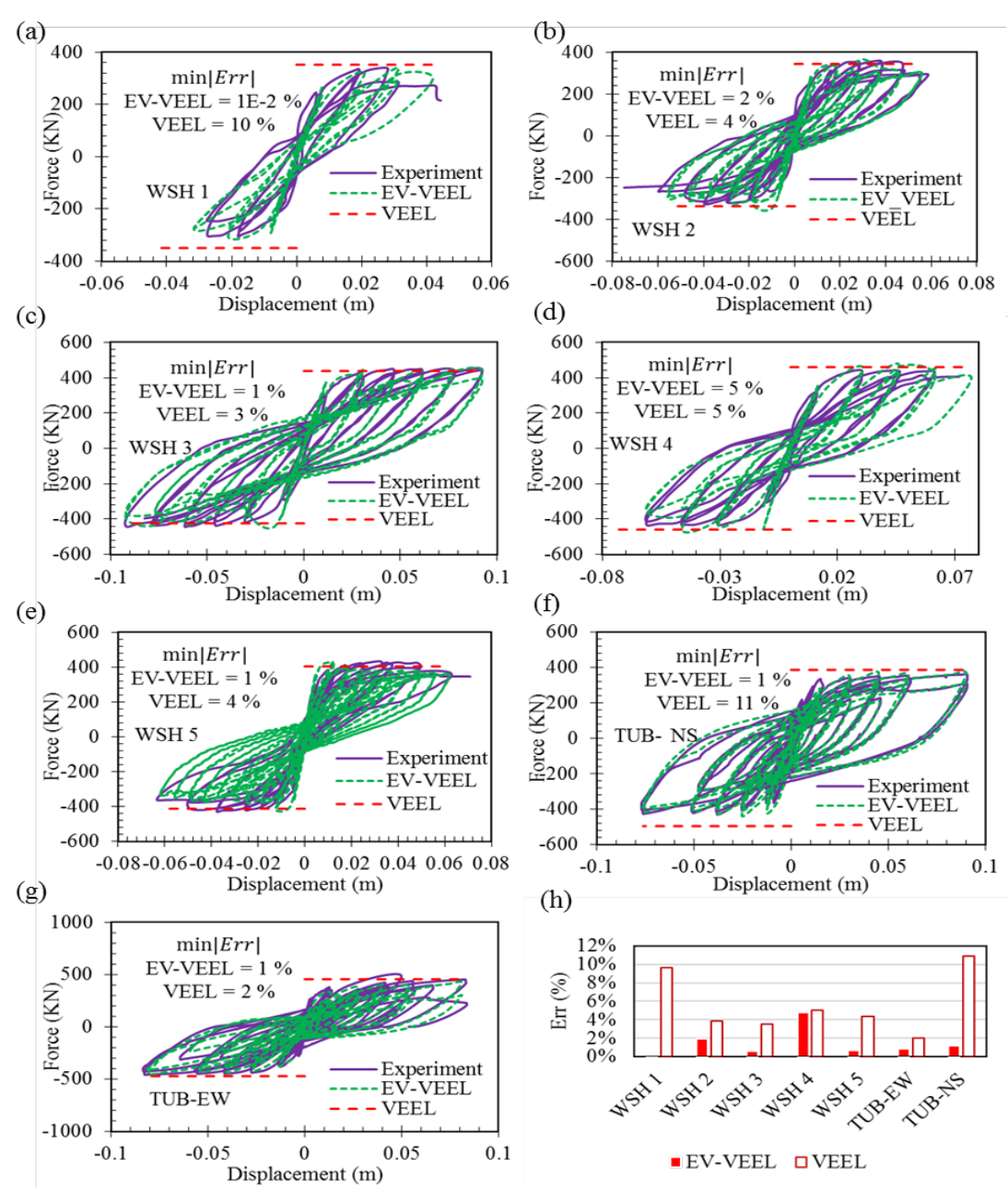


Fig. 20. Comparison of the accuracy of the adopted framework and default VEEL in terms of force and displacement: (a) the best-so-far results for WSH 1 with least minimum error; (b)~(e) the best-so-far results of different specimens WSH 2 ~ WSH 5 for strengthening the glass-box framework; (f) the best-so-far results of north-south (NS) direction loading for the last specimen TUB used in the framework; (g) the best-so-far results of East-West (EW) direction loading for TUB; (h) summary of the comparison between glass-box framework (EV-VEEL) and default VEEL.

Table 8. Summary of glass-box framework results.

Wall	Finished	Max.	Max.	Best	Best	Max.	CPU	Min.
Type	(Minutes)	Gen.	Org.	Generation	Organism	Group	CFU	Err (%)
WSH 1	2524	3	100	0	58	10	160	0. 2
WSH 2	4560	3	100	1	91	20	320	1.9
WSH 3	4323	10	1000	2	761	20	320	0.6
WSH 4	3381	3	100	1	76	20	320	5.9
WSH 5	6332	3	100	1	25	10	160	0.6
TUB	7227	2	50	0	47	10	160	2.3

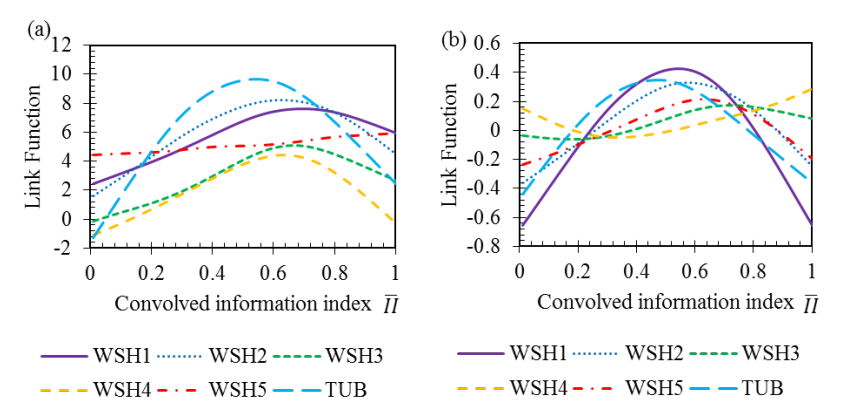


Fig. 21. Collecting coefficients through an LF: (a) β through convolved II; (b) C_{cs} for different walls.

7.3. CRS-based versus exponential LF's

In this section, two-parameter exponential LF and CRS-based LF have been used on WSH4 to compare the flexibility of the LF and ensure the accuracy of the proposed framework. As shown in Fig. 22, the minimum error in WSH 4 of exponential LF has changed slightly with the change of the α range. However, CRS-based LF, which contains less error than exponential LF, showed

more sensitivity to α range. Thus, it can be more applicable in delivering the material coefficients' mathematical relations due to the CRS form's multiple-parameter relationship.



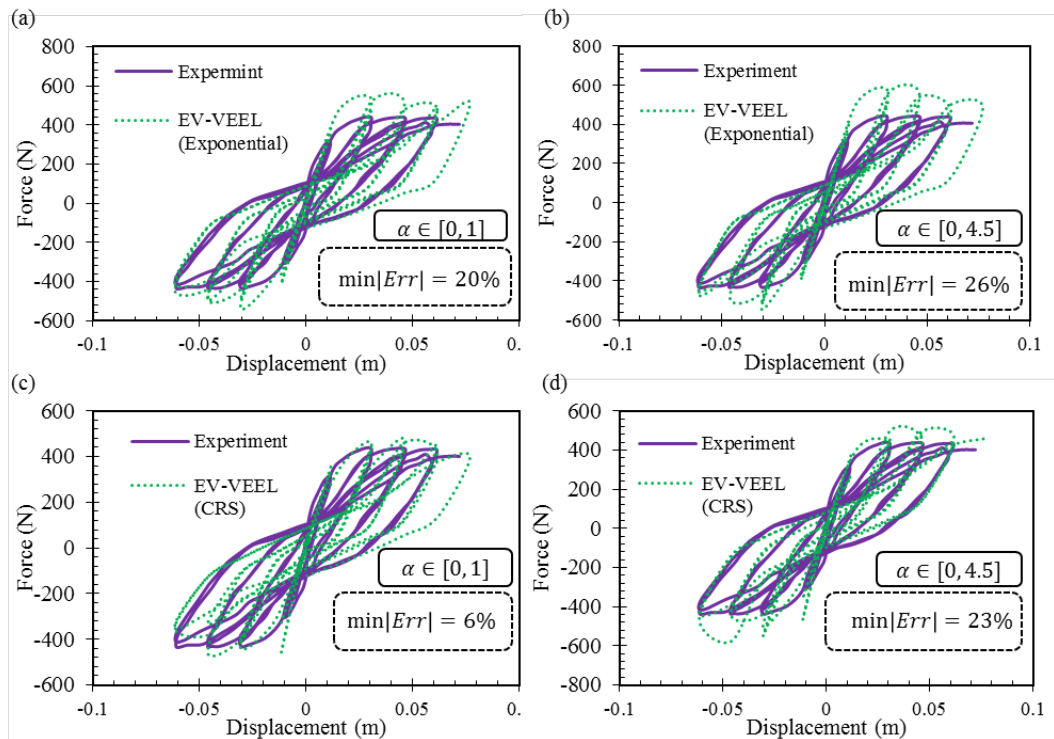


Fig. 22. Force-displacement of WSH 4 using different search ranges for α : (a) exponential LF with $\alpha \in [0, 1]$; (b) exponential LF with $\alpha \in [0, 4.5]$; (c) CRS-based LF with $\alpha \in [0, 1]$; (d) CRS-based LF with $\alpha \in [0, 4.5]$.

7.4. Generalization to 6 material models coefficients

The notable strength of the proposed glass-box framework lies in its expandability. It is highly facile to expand the learning core to include more new material coefficients. The glass-box framework's evolutionary algorithm is long gene-based storage that can be easily extended by adding more gene expressions for more material models (Fig. 23).

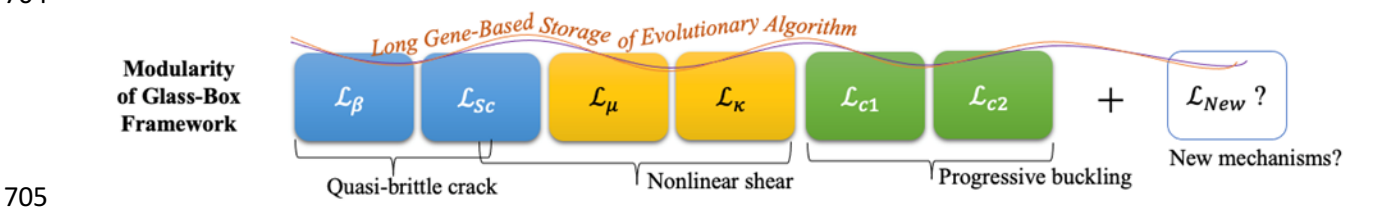


Fig. 23. Schematic of expandable gene-based storage of the evolutionary algorithm of the proposed glass-box framework.

To demonstrate the favorable expandability, this section extended the glass-box framework by including the 6-coefficients model (Model II) and comparing the accuracy to the default VEEL and 2-coefficients model (Model I). Then, each wall's prior best has been used to test a U-shaped wall, TUB (Fig. 24, Fig. 25, Table 9). First, WSH5 results show that the minimum error of the best-so-far generation of WSH5 in Model II, which is 0.6%, is less than the default VEEL (4.3%) and Model I (0.73%). Also, using the prior best of WSH5 for testing TUB shows better accuracy in Model II than using Model I and default VEEL, in which the minimum error using Model II is 3.1% while it is 6.5% and 3.9% with using default VEEL and Model I, respectively. However, the results of WSH3 show less accuracy, which the minimum error of the best-so-far generation is 2.3% with using 10 generations and 500 organisms, while the default VEEL (4.0%) and Model I are 4.0% and 2.13%, respectively. Also, the test of TUB using the prior best of WSH3 shows promising results in using Model II, in which the minimum error is 4.3% using Model II while it is 3.9% in Model I. Generally, it should be noted that increasing generations and organisms

increase the accuracy, but it costs more computational time and computing memory.

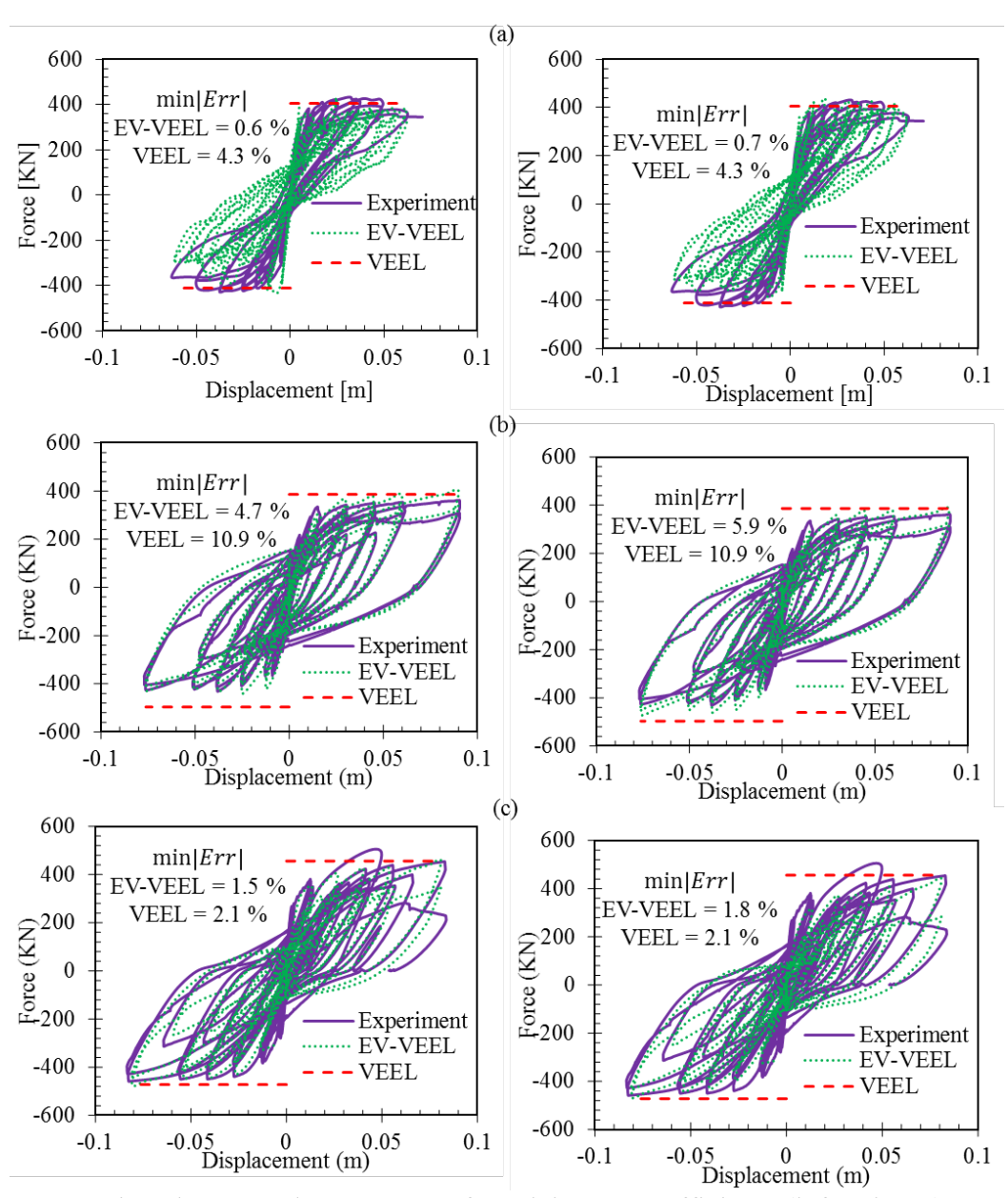


Fig. 24. Comparison between the accuracy of Model II: 6- coefficients (left column), Model I: 2-coefficients (right column), and default VEEL for the walls WSH5 and TUB in terms of force and displacement: (a) the best-so-far results for WSH 5 with the least minimum error; (b) the best-so-far results of north-south (NS) direction loading for TUB; (c) the best-so-far results of east-west (EW) direction loading for TUB.

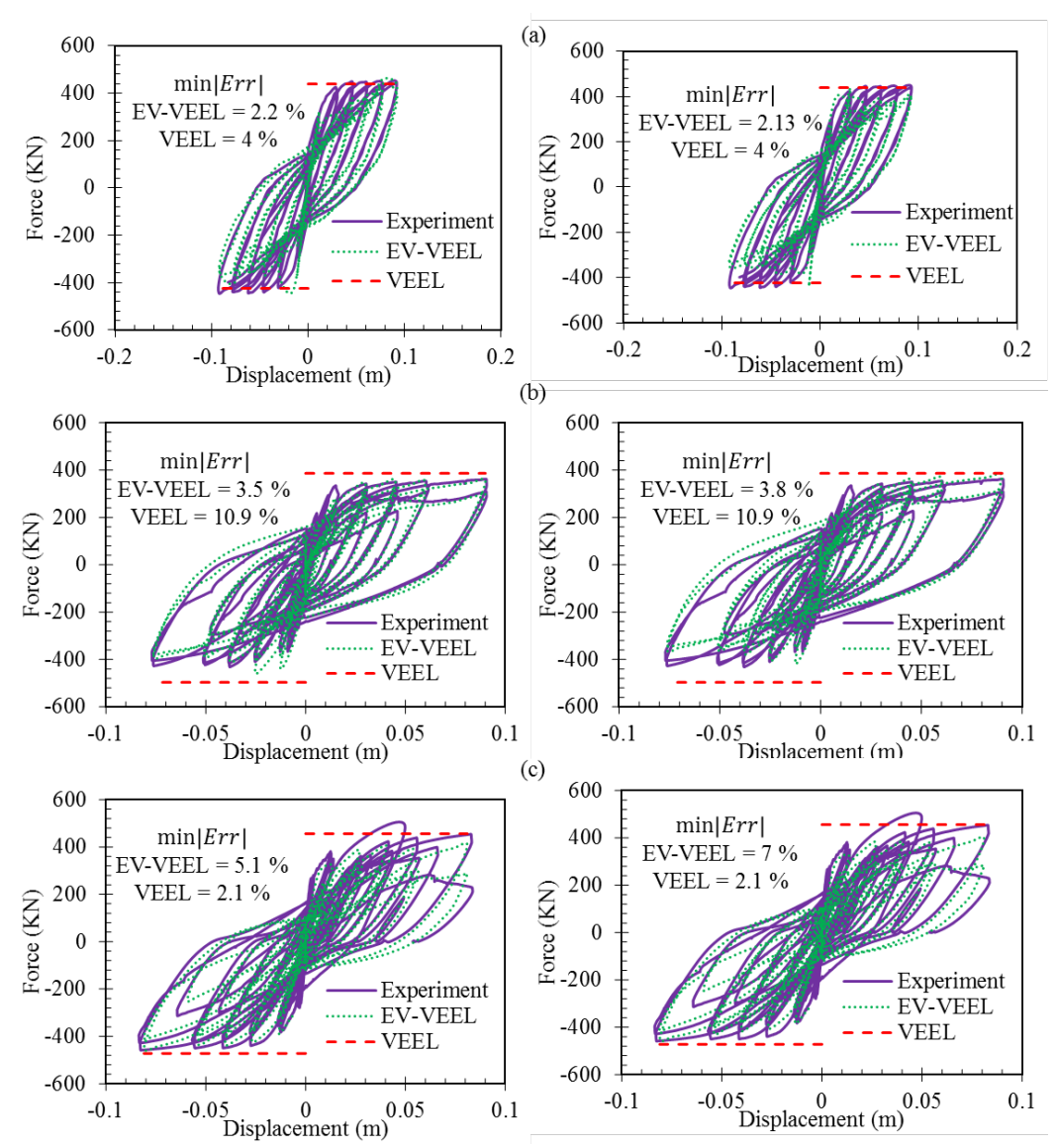


Fig. 25. Comparison between the accuracy of Model II: 6- coefficients (left column), Model I: 2-coefficients (right column), and default VEEL for the walls WSH3 and TUB in terms of force and displacement: (a) the best-so-far results for WSH 3 with the least minimum error; (b) the best-so-far results of north-south (NS) direction loading for TUB; (c) the best-so-far results of east-west (EW) direction loading for TUB.

Table 9. Validation results using default VEEL, Model I, and Model II.

337 11	Max.	Max	default	Model I: 2-Coeffs	Model II: 6-Coeffs	
Wall name	Generations	Organisms	VEEL Err [%]	Min. Err [%]	Min. Err [%]	
WSH3	10	500	4.0	2.13	2.2	
WSH5	3	100	4.3	0.73	0.6	
TUB (best WSH3)	1	10	(5	5.4	4.3	
TUB (best WSH5)	1	10	6.5	3.9	3.1	

Another important aspect of the proposed approach is the accessibility to detailed nonlinear damage behaviors of complex composite structures. As shown in Fig. 26, the proposed framework can directly access the microscopic nonlinear damage phenomena by capturing the compressive buckling of longitudinal reinforcing bars associated with concrete crushing and spalling. Such detailed damage responses are hard to capture by conventional computational analyses. Progressive buckling occurs (Fig. 26 d-g) in the combined effects of damages of surrounding quasi-brittle materials (Fig. 26 b-c; a large portion is spalled out or crushed out). The progressive buckling behavior is captured by the proposed approach by integrating all the damage information of surrounding materials and steel materials' current hysteretic stress-strain history.

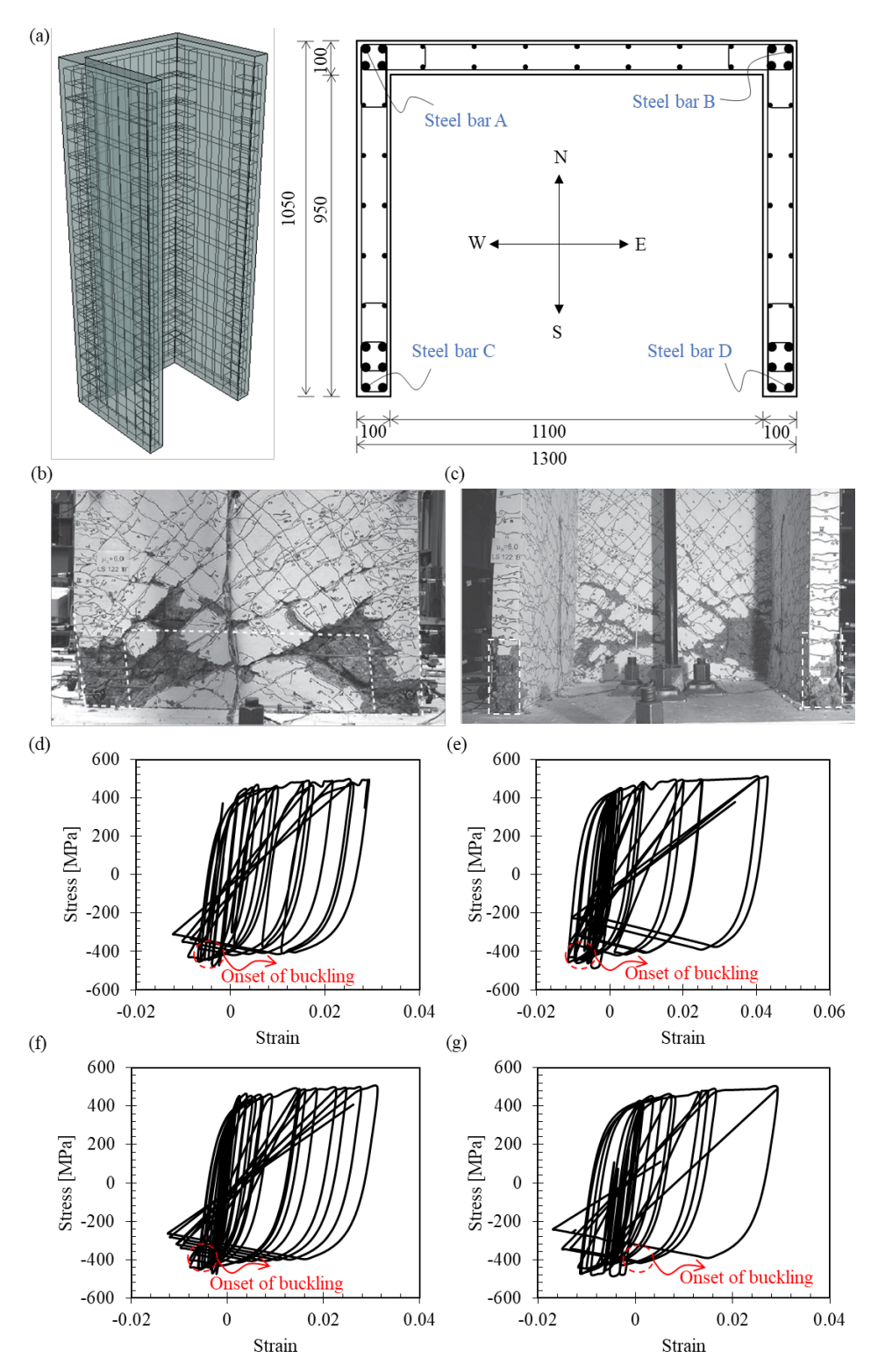


Fig. 26. The predicted responses of longitudinal steel bars depending on their locations: (a) cross-section of TUB (all dimensions are in mm); (b) concrete damage state at the north face of TUB; (c) concrete damage state at the south face (b and c are cited from Beyer et al. [49]); (d) stress-strain of steel bar A, (e) of steel bar C, (f) of steel bar B, and (g) of steel bar D.

7.5. Gradual Evolution Confirmed by a Simple Column Experiment

In this section, a composite hollow column (experimented by Cho [51]) has been analyzed to quantitatively demonstrate the gradual evolution. The material properties and geometric details are given in Table 10 and Fig. 27a. The hollow column (denoted as H40-300) is loaded by horizontal cyclic displacement loadings at the top and subjected to a constant axial force equivalent to 10% of the cross-sectional strength. As shown in Fig. 27b, the evolution via a combination of the Bayesian update and the genetic algorithm gradually improves the learning of the best-so-far rules for the material parameters of the mechanisms: i.e., gloal error decreases from 1.42% to 0.27%.



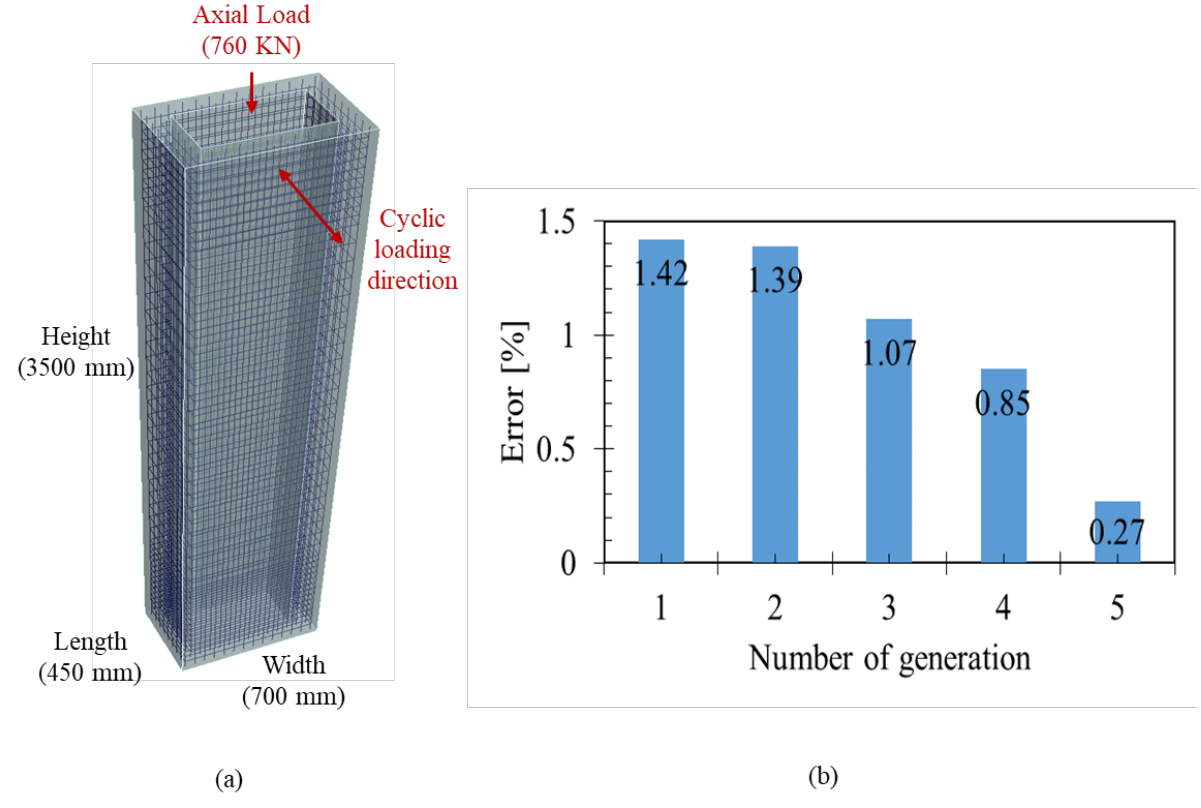


Fig. 27. The hollow column denoted as H40-300: (a) the geometry and details of the hollow column; (b) the best result of each generation to show the gradual evolution.

Table 10. Material properties of the hollow column (H40-300).

Concrete				Longitud	dinal bar		Hoop		
Compressive	Module of	Strain at	Tensile	Strain	Diameter	Yielding	Diameter	Spacing	Yielding
strength	elasticity	compressive	strength	at		stress		(mm)	stress
(MPa)	(MPa)	strength	(MPa)	tensile	(mm)	(MPa)	(mm)	(111111)	(MPa)
42.2	27,300	0.002	4.2	0.00014	10	350	6	50 or 100	350

8. Conclusion

- This paper describes how to generalize the glass-box computational material framework by proposing a new material-oriented convolved information index (denoted as \overline{II}_b) and highly flexible cubic regression spline (CRS)-based link function (LF), and the conclusion can be summarized as follow.
 - The proposed framework can honor and leverage the existing material models by selectively replacing the decisive material coefficients by LF and the convolved II.
 - The new convolved information index (II) introduced for nonlinear shear and progressive bar buckling mechanisms demonstrates the successful expandability of the proposed framework.
 - Virtual stress-based convolved II helps the proposed framework to leverage complex internal material heterogeneity and diverse BC's inside the large-scale structures.
 - CRS-based LFs appear more flexible and accurate than exponential LF. In particular, CRS-based LFs are able to describe the hidden rules behind the six target mechanisms' decisive material coefficients: i.e., the confinement-induced strength enhancement (β), three-dimensional interlocking-based nonlinear shear strength (C_{cs} and μ), the progressive compressive buckling of reinforcing bars (c_1 , c_2 , κ).
 - A variety of feasibility tests with large-scale reinforced composite structures confirmed that CRS-based LFs can outperform the manually calibrated high-fidelity simulations.

The next steps should include in-depth mathematical, analytical, and computational investigations. It shall be about the impact of flexible CRS bases on the adopted evolutionary algorithms and the favorable settings of the hyper-parameters (i.e., parameters related to the global learning algorithm's settings) of glass-box learning cores. Also, there should be a study on the effect of the sequence of the training specimens (i.e., complex specimen to the simple one, or independent of the complexity of specimens) on the context of the Bayesian update. Another important issue may be the inclusion of many advanced physical mechanisms at other scientific domains or diverse length scales from macro, micro, and even nano-scale (Cho et al. [52]).

Appendix

A. Introduction to the Convolutional Neural Network

The convolutional neural network (CNN) is a class of artificial neural networks that can be highly successful in practical applications such as image processing, learning and predicting continuous signals, and data classification (Oord et al. [53]; Raissi et al. [54]; Lee and Carlberg [55]). The structure of CNN is similar to the standard neural network, in which it includes convolutional layers, pooling layers, and fully connected layers (Fig. 2). First, the convolutional layer can obtain a set of feature maps which is the output of a mathematical operation between two inputs: an image matrix and a feature detector called a filter that can extract the optimum features from the input data. Then, the pooling layers simplify the information passed from the convolutional layer and reduce the scale of feature maps; hence, these layers can reduce computation and overfitting as there are only some parameters. In the pooling layers, many operations can be used, such as max-pooling, average-pooling, and min-pooling. Finally, the output of the previous procedures is fed into the fully connected layers, which contain the activation functions and the neurons, to classify and form the final output. The output of each neuron can be obtained by

813
$$a^{(l+1)} = f\left(\sum_{j=1}^{n_l} W_{i,j}^{(l)} x_j + b_i^{(l)}\right)$$
 (A. 1)

where $a^{(l+1)}$ is the output of the neuron; $W_{i,j}^{(l)}$ is the weight in layer (*l*) from neuron *j* to *i*; x_j is the

- input of the neuron j; $b_i^{(l)}$ is the bias term; f(.) is an activation function.
- For measuring the performance of the model, a cost/loss function is applied to compare the
- predicted output to the target output, which can be defined as

818
$$J(\mathbf{W}, \mathbf{b}) = Err + \lambda g(\mathbf{W}) \tag{A.2}$$

- where $I(\mathbf{W}, \mathbf{b})$ is the cost function that can return the error between predicted results compared
- with the actual results; Err is a prediction error; λ is a weight decay term for a function of W;
- 821 $g(\mathbf{W})$ can be squared sum of $W_{i,j}$ to prevent overfitting.
- Then, the backpropagation process can feed the cost value backward to minimize the cost value
- iteratively. For the minimization, the cost gradient $\nabla_{\mathbf{W}^{(l)}} J$ can be defined as

824
$$\nabla_{\mathbf{w}^{(l)}} I = \boldsymbol{\delta}^{(l+1)} \boldsymbol{a}^{(l)} \tag{A.3}$$

- where δ and α are the terminal error term and the activation at the associated layer. This leads to
- a gradient $\Delta \mathbf{W}^{(l)} = \Delta \mathbf{W}^{(l)} + \nabla_{\mathbf{W}^{(l)}} J$, and ultimately leads to update $\mathbf{W}^{(l)} = \mathbf{W}^{(l)} \alpha [\Delta \mathbf{W}^{(l)} + \nabla_{\mathbf{W}^{(l)}} J]$
- 827 $\lambda \mathbf{W}^{(l)}$ where α controls learning speed.

828

829

B. Literature review of ML-based RC structure applications

- There are many attempts to apply ML methods to the global structural level. Mangalathu et al.
- [56] used Naive Bayes, K-Nearest Neighbors, Decision Tree, and Random Forest to determine the
- failure mode of shear walls. Lee and Lee [57] presented an artificial neural network (ANN) to
- predict the shear strength of slender fiber-reinforced polymer reinforced concrete flexural
- members without stirrups. Abundeh et al. [58] used ML techniques to predict and study the

ANN algorithms to determine the influence of the structural parameters observed in earthquakes. Luo and Paal [60] presented an ML model to predict backbone curves used to evaluate the force-deformation behavior subjected to cyclic loading. Tsai and Hsu [61] used the backpropagation neural network technique to detect the RC structural damages. Jeng and Mo [62] presented a methodology to predict the early seismic response of prestressed concrete bridges by using ANN.

Table B.1. Literature summary of ML-based RC structure analyses.

Authors	Samples	variables	Target	Accuracy	Comments
Mangalathu et al. [56]	393 Shear walls	14	The failure mode of shear walls	*P.A. = 86%	The target is four categories of failure mode (Shear '1', flexure '2', flexure-shear '3', sliding '4').
					$P.A. = \hat{n}/N$, where \hat{n} is the number of correct failure mode predictions, and N is the total failure mode predictions.
S. Lee, C. Lee [57]	106 RC members	6	Shear strength	$R^2 = 0.95$	The authors used real experiment data of beams without stirrups to predict V_{cf} and then compare the results with empirical equations.
Abuodeh et al. [58]	120 RC Beams	15	Shear strength	$R^2 = 0.89$	The authors used real experimental data of beams to predict the shear strength of FRP V_f and then compare the results with design standards.
Arslan [59]	256 RC buildings	8	Displacement drift Capacity	$R^2 = 0.98$	Authors used pushover analysis results of real buildings to predict values for the global drift capacities at three performance levels (Immediate Occupancy 'IO', Life Safety 'LS', Collapse Prevention 'CP').
Luo and Paal [60]	262 Columns	15	Yield and maximum Shear force, drift values	$R^2 = 0.99$	Authors used real experimental data of columns to predict yield shear force V_y , drift ratio at yield shear δ_y , maximum shear force V_m , and drift ratio at maximum shear δ_m .

*P.A. is the prediction Accuracy.

C. Calculation procedure of virtual stress-based information index

This paper adopted the virtual stress-based information index (Cho [26]). Here, we summarize the key procedure to calculate the information index using virtual excitation, and further details can be found in Cho [26]. Every material point at $\mathbf{x} \in \Omega$, where Ω is the target structure's domain, is involved by virtual stress $\boldsymbol{\sigma}_{\mathbf{v}} = \langle \mathbf{I} \quad \mathbf{0} \rangle^T$, where $\mathbf{I} \in \mathbb{R}^3$ is the unity vector and $\mathbf{0} \in \mathbb{R}^3$ is zero

vector. A separate finite element analysis denoted as virtual FEA and eigenvalue analysis are performed to generate two virtual principal strain vectors.

The first virtual principal strain vector $\mathbf{\varepsilon}_{\mathrm{VI,pr}}^{(m)} \in \mathbb{R}^3$, where $m=1,\ldots,n_{el}$, and n_{el} is the total finite elements, can carry realistic deformation under the virtual stress $\sigma_{\mathbf{V}}$ for the real constraints, and it can be obtained by eigenvalue analysis of strains from the virtual FEA. Within the system, a finite element's integration point at location $\boldsymbol{\xi} \in \mathbb{R}^3$ and virtual force vector $\mathbf{R}_{\mathbf{V}} \in \mathbb{R}^{N_{DOF}}$, where N_{DOF} is the total degree of freedom of the system, and it is assumed to be virtually provided by the virtual stress vector. $\mathbf{R}_{\mathbf{V}}$ can be calculated by a typical FE procedure as

$$\mathbf{R}_{\mathbf{V}} = \sum_{m=1}^{n_{el}} \int_{\mathbf{V}^{(m)}} \left\{ \mathbf{B}^{(m)} \right\}^{\mathsf{T}} \mathbf{\sigma}_{\mathbf{V}} \, dV^{(m)}$$
 (C. 1)

where $\mathbf{B}^{(m)}$ is the typical matrix of derivatives of shape functions. After that, a virtual FEA of the real system subjected to only $\mathbf{R}_{\mathbf{V}}$ with no other external forces is performed to obtain the virtual displacement vector $\mathbf{U}_{\mathbf{V}} \in \mathbb{R}^{N_{DOF}}$ and the element-wise displacement vector $\mathbf{U}_{\mathbf{V}}^{(m)}$. Then, at every integration point at location $\boldsymbol{\xi}$ of an element (m), the virtual initial strain vector under the realistic constraints $\boldsymbol{\varepsilon}_{\mathrm{VI}}^{(m)}(\boldsymbol{\xi}) \in \mathbb{R}^6$ can be calculated as

$$\mathbf{\varepsilon}_{\mathbf{V}\mathbf{I}}^{(m)}(\boldsymbol{\xi}) = \mathbf{B}^{(m)}(\boldsymbol{\xi})\mathbf{U}_{\mathbf{V}}^{(m)} \tag{C.2}$$

After that, by performing the eigenvalue analysis with $\boldsymbol{\varepsilon}_{VI}^{(m)}(\boldsymbol{\xi})$, the principal strain vector $\boldsymbol{\varepsilon}_{VI,pr}^{(m)}(\boldsymbol{\xi}) \in \mathbb{R}^3$ and the associated transformation matrix $\mathbf{T}_{VI,pr}^{(m)}(\boldsymbol{\xi}) \in \mathbb{R}^3$ can be obtained.

The second virtual principal strain vector $\mathbf{\varepsilon}_{v,pr}^{(m)} \in \mathbb{R}^3$, can carry the amount of free deformation under the virtual stress $\mathbf{\sigma}_{\mathbf{V}}$ and it can be obtained by transforming $\left\{ \left(\mathbf{D}^{(m)} \right)^{-1} : \mathbf{\sigma}_{\mathbf{V}} \right\}$ where $\mathbf{D}^{(m)}$ is the linear elastic material matrix. As the counterpart of $\mathbf{\sigma}_{\mathbf{V}}$, we have the virtual strain vector $\mathbf{\varepsilon}_{\mathbf{V}}^{(m)}(\xi) \in \mathbb{R}^6$ that can be calculated with a linear elastic material matrix $\mathbf{D}^{(m)}(\xi)$ as

$$\boldsymbol{\varepsilon}_{V}^{(m)}(\boldsymbol{\xi}) = \left\{ \left(\mathbf{D}^{(m)}(\boldsymbol{\xi}) \right)^{-1} \right\} \boldsymbol{\sigma}_{V}$$
 (C. 3)

Hence, the second principal strain can be obtained by

875

873
$$\mathbf{T}_{VI,pr}^{(m)}(\xi)\boldsymbol{\varepsilon}_{V}^{(m)}(\xi) = \left\{\boldsymbol{\varepsilon}_{v,pr}^{(m)}(\xi), \boldsymbol{\gamma}_{v,pr}^{(m)}(\xi)\right\}$$
(C. 4)

where $\gamma_{\rm v,pr}^{(m)}(\xi) \in \mathbb{R}^3$ is the shear strain vector, which is negligible.

D. Calculation procedure of monotonic increasing link function

- The range of the parameters of \mathcal{L}_M in monotonic increasing can be obtained by applying the general
- mathematical condition to find the maximum of a linear function.

879
$$\frac{d\mathcal{L}_{M}}{dx}\Big|_{x_{max}=1.0} \ge 0 \Rightarrow a_{2} + a_{3}\dot{b_{3}}(x_{max}) + a_{4}\dot{b_{4}}(x_{max}) + a_{5}\dot{b_{5}}(x_{max}) \ge 0$$
 (D. 1)

where $\acute{b}_t(x_{max})$ is the first derivative of the basis functions that can be calculated. The other equation that can be used to obtain LF parameters is the general equation of LF $\mathcal{L}_M(x_{max}=1.0)=$ $\mathcal{L}_{M_{max}}$, where $\mathcal{L}_{M_{max}}$ is the maximum target LF that can be given by domain knowledge. It is not easy to solve these two equations with five unknowns; therefore, three more equations can be suggested from trial and error and the properties of basis functions individually. First, because a_1 and a_2 correspond to global shifting and linear increasing of LF, they are assumed to be equivalently dominant.

887
$$a_1 = \frac{\mathcal{L}_{M_{max}}}{2}; \ a_2 = \frac{\mathcal{L}_{M_{max}}}{2}$$
 (D.2)

The other suggested equation is assuming a_5 to be equal to the maximum target. Since the fifth basis function b_5 locates the maximum at x = 1 or 0 (see Fig. 11a). Hence, a_5 can be obtained as

890
$$a_5 = \frac{\mathcal{L}_{M_{max}}}{b_5(1.0)} \tag{D.3}$$

By solving the equation of $\mathcal{L}_M(x_{max})$ for a_3 and solving Eq. D.1 for a_4 , we can have the maximum

892 initial range of a_3 and a_4 as

897

898

893
$$a_3 = \frac{-\mathcal{L}_{M_{max}}}{b_3(1.0)} - \frac{b_4(1.0)}{b_3(1.0)} a_4; \ a_4 \le \frac{-A_{11}}{B_{11}}$$
 (D.4)

where A_{11} and B_{11} are constants that can be calculated as

895
$$A_{11} = \left(\frac{\mathcal{L}_{M_{max}}}{2}\right) + \left(\dot{b_3}(1.0)\frac{-\mathcal{L}_{M_{max}}}{b_3(1.0)}\right) + \left(\frac{\dot{b_5}(1.0)\mathcal{L}_{M_{max}}}{b_5(1.0)}\right)$$
(D. 5)

896
$$B_{11} = b_4'(1.0) - \frac{b_4(1.0)}{b_3(1.0)}b_3'(1.0) \tag{C.6}$$

E. Calculation procedure of convex link function

The conditions are slightly changed when the maximum target is located at the middle ($\hat{x} = 0.5$).

Herein, the range of the parameters of \mathcal{L}_M can be obtained by applying the first and second

901 derivatives to find the local maximum where the slope is zero.

902
$$\frac{d\mathcal{L}_M}{dx}\Big|_{\hat{x}=0.5} = 0 \Rightarrow a_2 + a_3 \dot{b_3}(\hat{x}) + a_4 \dot{b_4}(\hat{x}) + a_5 \dot{b_5}(\hat{x}) = 0$$
 (E.1)

903
$$\frac{d^2 \mathcal{L}_M}{dx^2} \bigg|_{\hat{x}=0.5} < 0 \Rightarrow a_3 b_3^{"}(\hat{x}) + a_4 b_4^{"}(\hat{x}) + a_5 b_5^{"}(\hat{x}) < 0$$
 (E.2)

where $b_i(x) = db_i(x)/dx$, and $b_i''(x) = d^2b_i(x)/dx^2$, as shown in Fig. 11b and Fig. 11c. Still,

905 there are three equations with five unknowns. As before, being equivalently dominant, a_1 and a_2

are assumed to be equal at $\hat{x} = 0.5$, and they can be obtained as

907
$$a_1 = \frac{\mathcal{L}_{M_{max}}}{4}; \ a_2 = \frac{\mathcal{L}_{M_{max}}}{2}$$
 (E.3)

Substituting Eq. E.3 into Equations E.1, E.2 and $\mathcal{L}_M(\hat{x})$ to obtain a_3 , a_4 , and a_5 as

909
$$a_3 = (C_{11} - D_{11}E_{11}) - (D_{11}F_{11})a_5$$
 (E.4)

910
$$a_4 = E_{11} - F_{11}a_5 \tag{E.5}$$

911
$$a_{5} > \frac{(C_{11} - D_{11}E_{11})b_{3}^{"}(\hat{x}) + E_{11}b_{4}^{"}(\hat{x})}{(b_{5}^{"}(\hat{x}) - D_{11}F_{11}b_{3}^{"}(\hat{x}) - F_{11}b_{4}^{"}(\hat{x}))}$$
 (E. 6)

912 where $C_{11} \sim F_{11}$ are constants that can be defined as

913
$$C_{11} = -\frac{\mathcal{L}_{M_{max}}}{4b_2(\hat{x})\dot{b}_3(\hat{x})}; D_{11} = \frac{\dot{b}_4(\hat{x})}{\dot{b}_3(\hat{x})}$$
(E.7)

914
$$E_{11} = \frac{\mathcal{L}_{M_{max}} b_3(\hat{x}) - 2\mathcal{L}_{M_{max}} b_2(\hat{x}) \dot{b}_3(\hat{x})}{4b_2(\hat{x}) [b_3(\hat{x}) \dot{b}_4(\hat{x}) - \dot{b}_3(\hat{x}) b_4(\hat{x})]}; F_{11} = \frac{\left[\dot{b}_5(\hat{x}) b_3(\hat{x})\right] - \left[\dot{b}_3(\hat{x}) \dot{b}_5(\hat{x})\right]}{b_3(\hat{x}) \dot{b}_4(\hat{x}) - \dot{b}_3(\hat{x}) b_4(\hat{x})}$$
(E. 8)

F. Scalability of the Adopted Parallel Grouping Algorithm

- The proposed framework requires many organisms, along with high-precision computational material models, to perform reliable learning and evolution. However, a full GA has a global iteration for many organisms, which is an "embarrassingly parallelizable" process. To handle many organisms concurrently, we apply a CPU group technique for a separate parallel multi-scale
- 921 FEA.

915

- Let SG_i , $i=1,...,n_{SG}$ be a subgroup of CPUs, which performs the computation of a portion of
- organisms. Each CPU group has $M_{org}^{(SG_i)}$ such that

924
$$M_{org} = \sum_{i=1}^{n_{SG}} M_{org}^{(SG_i)}; \qquad G_{CPU} = \bigcup_{i=1}^{n_{SG}} SG_i$$
 (F. 1)

- where $G_{CPU} = \{P_0, P_1, ..., P_{n-1}\}$ in size of p is the set of all available processors, and $SG_i = \{P_0, P_1, ..., P_{n-1}\}$
- 926 $\left\{P_0^{(SG_i)}, P_1^{(SG_i)}, \dots, P_{p_{(i)}-1}^{(SG_i)}\right\}$ is the i_{th} subgroup of processors in size of $p_{(i)}$.

$$p_{(i)} = \begin{cases} p_{avg} & (i < n_{SG}) \\ p - p_{avg} & (i = n_{SG}) \end{cases}$$
 (F.2)

- where $i=1,...,n_{SG}$ and $p_{avg}=floor\left(\frac{p}{n_{SG}}\right)-1$; The authors' dedicated work in large and
- omplex parallel multi-scale FEAs (Cho and Porter [39]; Cho and Hall [40]; Cho [26]) proved the

power of multi-layered CPU grouping parallelism. As shown in Fig. F.1a, it briefly illustrates the architecture of the multi-layered parallelism. In general, each CPU subgroup handles M_{org}/n_{SG} organisms. The platform used in the paper for all the parallel computers is Condo 2017 of Iowa State University, consisting of 192 SuperMicro nodes. Each node has two 8-core Intel Haswell processors, 128GB of memory, and a 2.5 TB local disk.



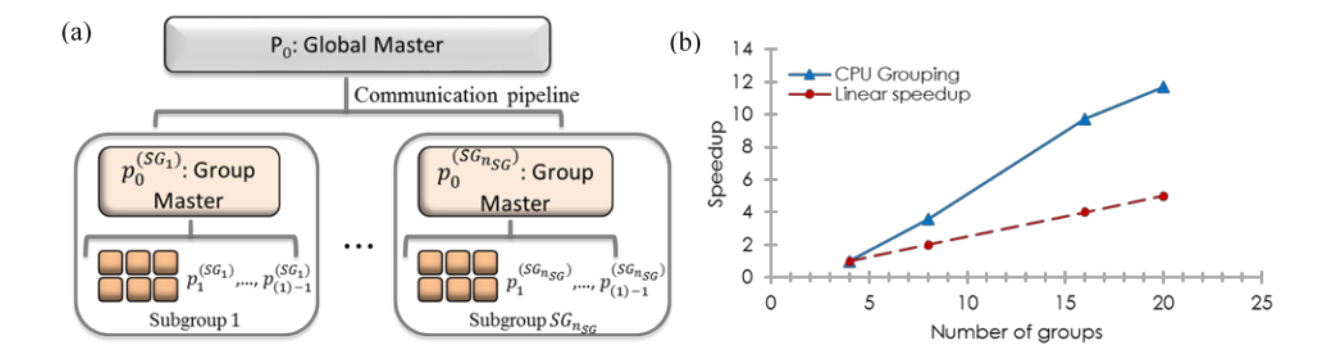


Fig. F.1. (a) the architecture of hierarchical and multi-layered CPU grouping techniques. The global master only communicates with the hierarchical group masters in the pipeline; (b) super speedup of CPU grouping technique based on wall-clock time for learning one generation of 80 organisms by varying number of groups n_{SG} . Running time is normalized by that of 4 subgroups (i.e., 26722 seconds).

In Fig. F.1b, the CPU grouping technique appears to exhibit a seemingly 'super speedup' (i.e., faster than the ideal linear speedup) by distributing the expensive computational cost of individual parallel multi-scale FEA. The authors' dedicated work in Cho and Porter [39] theoretically explains the seemingly super-linear speedup of the present multi-layered parallel multi-scale analysis. In Table F.1, each subgroup has a fewer number of CPUs as the number of groups increases. One of the reasons for this promising performance is communication reduction due to the Condo cluster system's shared memory since the intra-node transfer cost is typically smaller than the inter-node transfer cost.

Table F.1. The number of CPUs (i.e., $p_{(i)}$) in the *ith* subgroup of CPUs by a varying number of groups n_{SG} . The total number of CPUs (i.e., p) is fixed as 320.

	$n_{SG}=4$	$n_{SG}=8$	$n_{SG}=16$	$n_{SG}=20$
$p_{(i)}$	80	40	20	16
Time (sec)	26,722	7,489	2,747	2,287

Suppose we have access to the cloud computing environment. In that case, the proposed program can handle many organisms to optimize the link function between the computational material models and the information index.

G. Statistical Application Examples using Generalized Additive Model

Previous researchers applied genetic programming to find a functional relationship between the features in data to the target (e.g., Solhmirzaei et al. [14]). In a similar fashion, researchers can derive a statistical prediction model of a target behavior by coupling the best-so-far evolving VEEL with an advanced statistical method. As a practical example, a generalized additive model (GAM) is used to derive a statistical model of the maximum shear force of rectangular walls using CRS. In general, GAM is a non-parametric regression model that can depend on the sum of undetermined smooth functions (Hastie and Tibshirani [27]; Wood [28]; Song et al. [63]), and the general form of GAM is given by Eq. 14. In this example, the statistical prediction is performed on training data, containing 283 instances, seven descriptive variables, and one target variable. These 283 instances are generated by the evolving VEEL with the best-so-far setting as of the date of simulation. The training was performed on the training dataset (70% of the full data, 198 instances). The final identified statistical model based on GAM can be written in the open-source statistics program *R* as

973
$$F_{Max} = gam(FS \sim s(L, bs = "cr", k = 7) + s(Th, bs = "cr", k = 7) + s(H, bs = "cr", k = 7)$$
974
$$+ s(AFR, bs = "cr", k = 7) + s(Fc, bs = "cr", k = 7) + s(Fy, bs = "cr", k = 7)$$
975
$$+ s(D, bs = "cr", k = 7), family = Gamma(link = "log"), data = trainset)$$

where this study uses the Gamma distribution which is suitable for the nature of data (real and positive values), and we use the logarithmic link of GAM. In addition, the number of basis dimensions in smooth functions (k) has been chosen to be seven as recommended by literature (e.g., Wood [28]). The instances of concrete shear walls can be described by different variables (Table G.1). The results of the statistical training is shown in Fig. G.1.

Table G.1. Variable Characteristics

Variables	Detail
L	Length of shear wall
Th	Thickness of shear wall
Н	Height of shear wall
AFR	Axial force ratio
Fc	Concrete compressive strength
Fy	Yield strength of longitudinal reinforcement
D	Diameter of boundary longitudinal reinforcement
FS	Maximum shear force



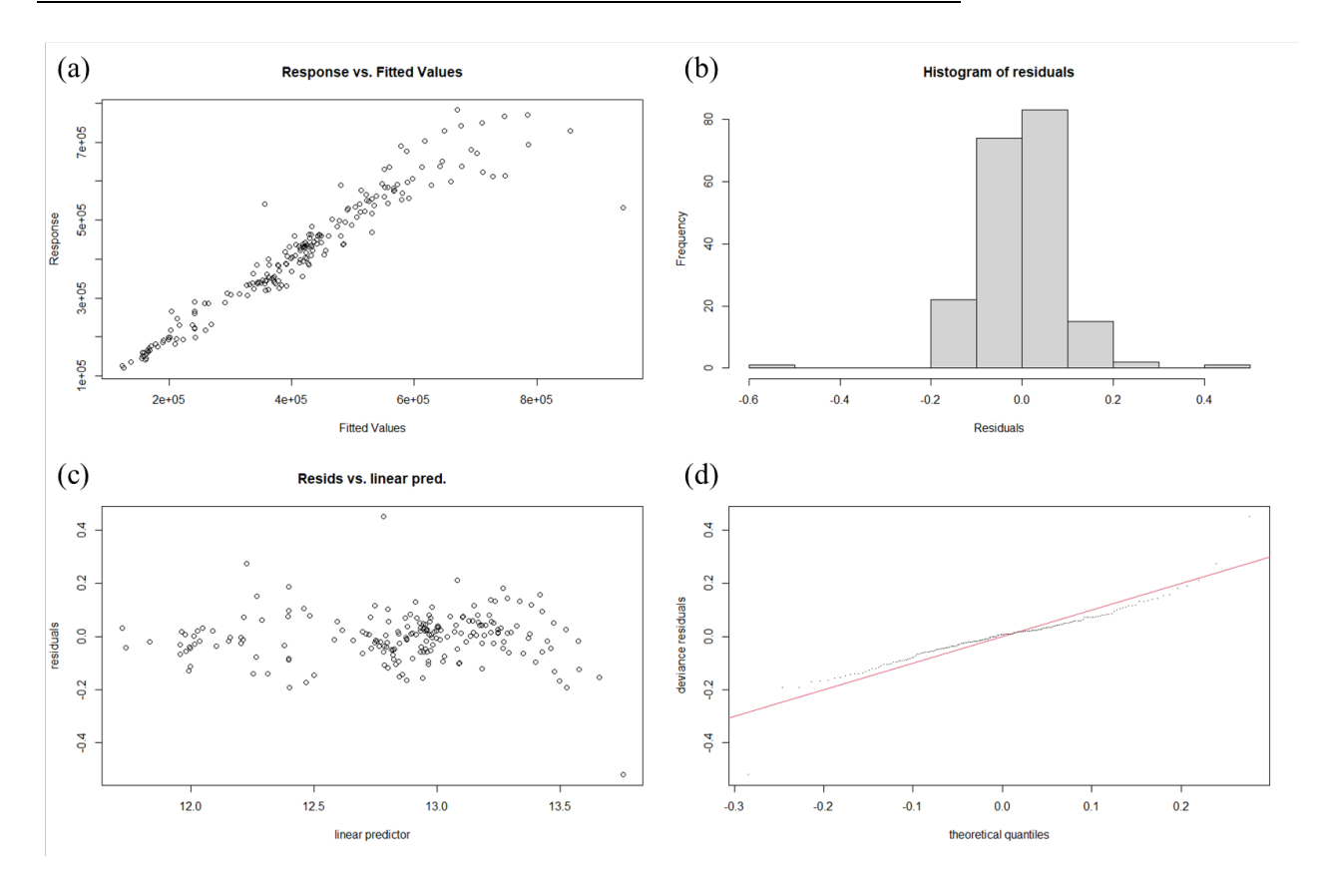


Fig. G.1. The results of the training dataset. (a) response vs. fitted values; (b) Histogram of residuals; (c) residuals vs. linear predictor; (d) Q-Q plot.

With 30% test data set, the coefficient of determination (R^2) is calculated as 0.84 (Fig. G.2). It should be noted that this accuracy may not be the global optimal subject to further improvement by optimization of GAM itself (e.g., Song et al. [63]). Still, this example demonstrates well that the proposed evolved framework can be coupled with an advanced statistical method to obtain a practically useful statistical prediction model.

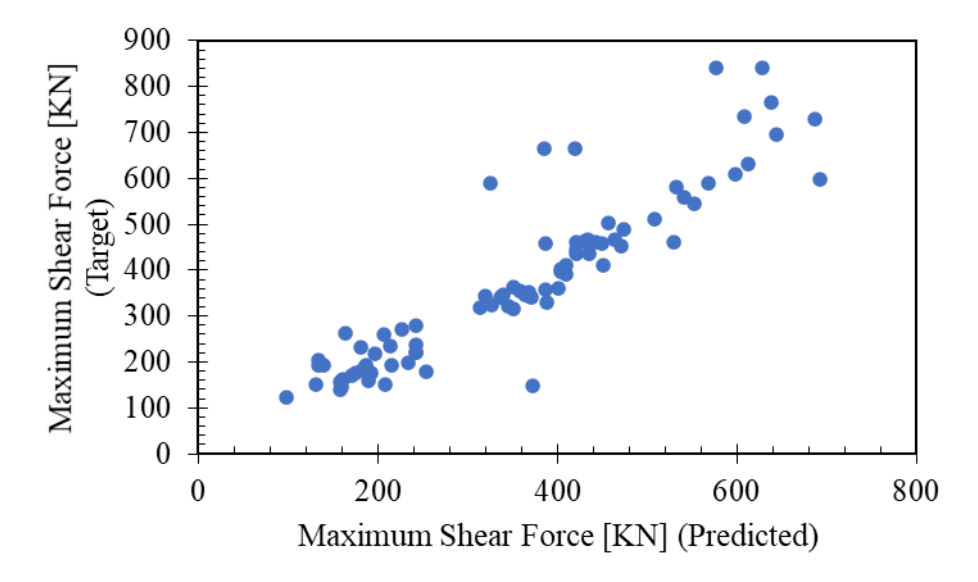


Fig. G.2. Prediction test against test dataset containing 30% of the full data (85 instances), resulting in $R^2 = 0.84$.

Acknowledgments

This research is, in part, supported by the research funding of the National Science Foundation under grant OAC-1931380, and the University of Jeddah-Saudi Arabia. The computational simulation reported in this paper is partially supported by the HPC@ISU equipment at Iowa State University, some of which have been purchased through funding provided by NSF under MRI grant number CNS 1229081and CRI grant number 1205413.

10041005 References

- 1006 [1] Hashash, Y. M. A., Jung, S., & Ghaboussi, J. 2004. "Numerical implementation of a neural network based material model in finite element analysis." *International Journal for numerical methods in engineering*, 59(7), 989-1005.
- [2] Koenuma, Kohta, Akinori Yamanaka, Ikumu Watanabe, and Toshihiko Kuwabara. 2020.
 "Estimation of Texture-Dependent Stress-Strain Curve and r-Value of Aluminum Alloy
 Sheet Using Deep Learning." *Materials Transactions* 61 (12): 2276-2283.
- 1012 [3] Vlassis, Nikolaos N., Ran Ma, and WaiChing Sun. 2020. "Geometric deep learning for computational mechanics Part I: Anisotropic Hyperelasticity." *Computer Methods in Applied Mechanics and Engineering* 371: 113299.
- [4] Logarzo, Hernan J., German Capuano, and Julian J. Rimoli. 2021. "Smart constitutive laws:
 Inelastic homogenization through machine learning." Computer Methods in Applied
 Mechanics and Engineering 373: 113482.
- [5] Masi, Filippo, Ioannis Stefanou, Paolo Vannucci, and Victor Maffi-Berthier. 2020.
 "Thermodynamics-based Artificial Neural Networks for constitutive modeling." *Journal* of the Mechanics and Physics of Solids 147: 104277.
- [6] Oh, B. K., Y. Park, and H. S. Park. 2020. "Seismic response prediction method for building structures using convolutional neural network." *Structural Control and Health Monitoring*.
 [7] Okazaki, Y., S. Okazaki, S. Asamoto, and P. J. Chun. 2020. "Applicability of machine learning
- to a crack model in concrete bridges." *Computer-Aided Civil and Infrastructure*Engineering.

- 1026 [8] Wu, R. T., and M. R. Jahanshahi. 2019. "Deep convolutional neural network for structural
- dynamic response estimation and system identification." Journal of Engineering
- 1028 *Mechanics* 145 (1): 04018125.
- 1029 [9] Cladera, A., and A. R. Mari. 2004. "Shear design procedure for reinforced normal and high-
- strength concrete beams using artificial neural networks. Part II: beams with stirrups."
- 1031 *Engineering Structures* 26 (7): 927-936.
- 1032 [10] Tehranizadeh, M., and M. Safi. 2004. "Application of artificial intelligence for construction
- of design spectra." *Engineering structures* 26 (6): 707-720.
- 1034 [11] Abdalla, J. A., Elsanosi, A., & Abdelwahab, A. 2007. "Modeling and simulation of shear
- resistance of R/C beams using artificial neural network." Journal of the Franklin
- 1036 *Institute*, 344(5), 741-756.
- 1037 [12] Abdalla, J. A., Saqan, E. I., & Hawileh, R. A. 2014. "Optimum seismic design of unbonded
- post-tensioned precast concrete walls using ANN." *Comput Concrete*, 13, 547-567.
- 1039 [13] Abuodeh, O. R., Abdalla, J. A., & Hawileh, R. A. 2020. "Prediction of shear strength and
- behavior of RC beams strengthened with externally bonded FRP sheets using machine
- learning techniques." *Composite Structures*, 234, 111698.
- 1042 [14] Solhmirzaei, R., Salehi, H., Kodur, V., & Naser, M. Z. 2020. "Machine learning framework
- for predicting failure mode and shear capacity of ultra high performance concrete
- beams." *Engineering structures*, 224, 111221.
- 1045 [15] Bessa, M. A., Z. Liu Bostanabad, Daniel W. Apley, C. Brinson, W. Chen, and Wing Kam
- Liu. 2017. "A framework for data-driven analysis of materials under uncertainty:
- 1047 Countering the curse of dimensionality." Computer methods in applied mechanics and
- 1048 *engineering* 320: 633-667.

- 1049 [16] Ma, Zhan, and Wenxiao Pan. 2021. "Data-driven nonintrusive reduced order modeling for
- dynamical systems with moving boundaries using Gaussian process regression." *Computer*
- 1051 *Methods in Applied Mechanics and Engineering* 373: 113495.
- 1052 [17] Kirchdoerfer, T., and M. Ortiz. 2016. "Data-driven computational mechanics." Computer
- 1053 *Methods in Applied Mechanics and Engineering* 304: 81-101.
- 1054 [18] Eggersmann, R., L. Stainier, M. Ortiz, and S. Reese. 2020. "Model-free data-driven
- 1055 computational mechanics enhanced by tensor voting." Computer Methods in Applied
- 1056 *Mechanics and Engineering* 373: 113499.
- 1057 [19] Patel, Ravi G., Nathaniel A. Trask, Mitchell A. Wood, and Eric C. Cry. 2020. "A physics-
- informed operator regression framework for extracting data-driven continuum models."
- 1059 [20] Cheng, M.Y., P.M. Firdausi, and D. Prayogo. 2014. "High-performance concrete compressive
- strength prediction using Genetic Weighted Pyramid Operation Tree (GWPOT)."
- 1061 Engineering Applications of Artificial Intelligence 29: 104-113.
- 1062 [21] Mozaffar, M., Bostanabad, R., Chen, W., Ehmann, K., Cao, J., & Bessa, M. A. 2019. "Deep
- learning predicts path-dependent plasticity." Proceedings of the National Academy of
- 1064 *Sciences*, 116(52), 26414-26420.
- 1065 [22] Abueidda, D. W., Koric, S., & Sobh, N. A. 2020. "Topology optimization of 2D structures
- with nonlinearities using deep learning." *Computers & Structures*, 237, 106283.
- 1067 [23] Chen, C. T., & Gu, G. X. 2020. "Generative deep neural networks for inverse materials design
- using backpropagation and active learning." *Advanced Science*, 7(5), 1902607.
- 1069 [24] Abueidda, D. W., Koric, S., Sobh, N. A., & Sehitoglu, H. 2021. "Deep learning for plasticity
- and thermo-viscoplasticity." *International Journal of Plasticity*, 136, 102852.

- 1071 [25] Kollmann, H. T., Abueidda, D. W., Koric, S., Guleryuz, E., & Sobh, N. A. 2020. "Deep
- learning for topology optimization of 2D metamaterials." *Materials & Design*, 196,
- 1073 109098.
- 1074 [26] Cho, I. 2019. "A framework for self-evolving computational material models inspired by deep
- learning." International Journal for Numerical Methods in Engineering 120 (10): 1202-
- 1076 1226.
- 1077 [27] Hastie, T., and R. Tibshirani. 1990. Generalized Additive Models. Chapman & Hall.
- 1078 [28] Wood, Simon N. 2006. Generalized additive models: an introduction with R. Boca Raton,
- 1079 FL: Chapman & Hall/CRC.
- 1080 [29] Wang, S. Y., K. Tai, and M. Y. Wang. 2006. "An enhanced genetic algorithm for structural
- topology optimization." *International Journal for Numerical Methods in Engineering* 65
- 1082 (1): 18-44.
- 1083 [30] Tang, W., L. Tong, and Y. Gu. 2005. "Improved genetic algorithm for design optimization of
- truss structures with sizing, shape and topology variables." *International Journal for*
- 1085 *Numerical Methods in Engineering* 62 (13): 1737-1762.
- 1086 [31] Johnson, J. M., and Y. Rahmat-Samii. 1999. "Genetic algorithms and method of moments
- 1087 (GA/MOM) for the design of integrated antennas." *IEEE Transactions on Antennas and*
- 1088 *Propagation* 47 (10): 1606-1614.
- 1089 [32] Waisman, H., E. Chatzi, and A. W. Smyth. 2010. "Detection and quantification of flaws in
- structures by the extended finite element method and genetic algorithms." *International*
- Journal for Numerical Methods in Engineering 82 (3): 303-328.
- 1092 [33] Koza, John R. 1992. Genetic Programming: On The Programming of Computers By Means
- 1093 *of Natural Selection.* MIT press.

- 1094 [34] Cho, I., and J. Hall. 2014. "General confinement model based on nonlocal information."
- 1095 *Journal of Engineering Mechanics* 140 (6).
- 1096 [35] Bazant, Z. P., and M. Jirasek. 2001. "Nonlocal integral formulation of plasticity and damage:
- survey of progress." *Journal of Engineering Mechanics* 128 (11): 1119-1149.
- 1098 [36] Rodriguez, M. E., J.C. Botero, and J. Villa. 1999. "Cyclic stress-strain behavior of reinforcing
- steel including effect of buckling." *Journal of Structural Engineering* 125 (6): 605-612.
- 1100 [37] Dhakal, R. P., and K. Maekawa. 2002. "Modeling for postyield buckling of reinforcement."
- *Journal of structural engineering* 128 (9): 1139-1147.
- 1102 [38] Cho, I. 2013. "Virtual earthquake engineering laboratory capturing nonlinear shear, localized
- damage and progressive buckling of bar." *Earthquake Spectra* 29 (1): 103-126.
- 1104 [39] Cho, I., and K. Porter. 2014. "Multi-layered grouping parallel algorithm for multiple-level
- multi-scale analyses." International Journal for Numerical Methods in Engineering 100
- 1106 (12): 914-932.
- 1107 [40] Cho, I., and F. Hall. 2012. "Parallelized Implicit Nonlinear FEA Program for Real Scale RC
- Structures under Cyclic Loading." *Journal of computing in civil engineering* 26 (3): 356-
- 1109 365.
- 1110 [41] Thorenfeldt, E. 1987. "Mechanical properties of high-strength concrete and applications in
- design." *In Symposium Proceedings, Utilization of High-Strength Concrete.*
- 1112 [42] Taucer, F., E. Spacone, and F. C. Filippou. 1991. "A fiber beam-column element for seismic
- response analysis of reinforced concrete structures." Earthquake engineering research
- 1114 *center* 91.
- 1115 [43] Reinhardt, H. W. 1984. "Fracture mechanics of an elastic softening material like concrete."
- 1116 *HERON* 29 (2).

- 1117 [44] Bazant, Z. P., and B. H. Oh. 1983. "Crack band theory for fracture of concrete." *Materiaux et*
- 1118 *Constructions* 16: 155-177.
- 1119 [45] Cho, I. 2018. "Deformation Gradient-Based Remedy for Mesh Objective Three-Dimensional
- 1120 Interlocking Mechanism." *ASCE Journal of Engineering Mechanics* 144 (1).
- 1121 [46] Jackson, R. L., and I. Green. 2006. "A statistical model of elasto-plastic asperity contact
- between rough surfaces." *Tribology International* 39 (9): 906-914.
- 1123 [47] Schmidt, M., and H. Lipson. 2009. "Distilling free-form natural laws from experimental data."
- science 324: 81-85.
- 1125 [48] Dazio, A., K. Beyer, and H. Bachmann. 2009. "Quasi-static cyclic tests and plastic hinge
- analysis of RC structural walls." *Engineering Structures* 31 (7): 1556-1571.
- 1127 [49] Beyer, K., A. Dazio, and M. J. N. Priestly. 2008. "Quasi-static cyclic tests of two U-shaped
- reinforced concrete walls." *Journal of earthquake engineering* 12 (7): 1023-1053.
- 1129 [50] Walraven, J. 1994. "Rough cracks subjected to earthquake loading." *Journal of Structural*
- 1130 Engineering 120 (5): 1510-1524.
- 1131 [51] Cho, K. 2004. "An experimental and analytical study on the seismic behavior of RC piers
- using high-strength concrete and high-strength rebars." (Doctoral dissertation, Seoul
- 1133 National Univ).
- 1134 [52] Cho, I., Li, Q., Biswas, R., and Kim, J., 2020. A Framework for Glass-Box Physics Rule
- Learner and Its Application to Nano-Scale Phenomena, Nature, Communications Physics
- 3, Article Number 78 [DOI:10.1038/s42005-020-0339-x].
- 1137 [53] Oord A, Dieleman S, Zen H, Simonyan K, Vinyals O, Graves A, Kalchbrenner N, Senior A,
- 1138 Kavukcuoglu K. 2016. "A generative model for raw audio." *Sound Mach, Learn*.

- 1139 [54] Raissi, M., Perdikaris, P., & Karniadakis, G. E. 2017. "Physics informed deep learning (part
- i): Data-driven solutions of nonlinear partial differential equations." arXiv preprint
- 1141 *arXiv:1711.10561*.
- 1142 [55] Lee, K., & Carlberg, K. T. 2020. "Model reduction of dynamical systems on nonlinear
- manifolds using deep convolutional autoencoders." Journal of Computational
- 1144 *Physics*, 404, 108973.

- 1146 [56] Mangalathu, S., H. Jang, S.H. Hwang, and J.S. Jeon. 2020. "Data-driven machine-learning-
- based seismic failure mode identification of reinforced concrete shear walls." *Engineering*
- 1148 *Structures* 208: 110331.
- 1149 [57] Lee, S., and C. Lee. 2014. "Prediction of shear strength of FRP-reinforced concrete flexural
- members without stirrups using artificial neural networks." *Engineering structures* 61: 99-
- 1151 112.
- 1152 [58] Abuodeh, Omar R., Jamal A. Abdalla, and Rami A. Hawileh. 2020. "Prediction of shear
- strength and behavior of RC beams strengthened with externally bonded FRP sheets using
- machine learning techniques." *Composite Structures* 234: 111698.
- 1155 [59] Arslan, M. Hakan. 2010. "An evaluation of effective design parameters on earthquake
- performance of RC buildings using neural networks." *Engineering Structures* 32.7: 1888-
- 1157 1898.
- 1158 [60] Luo, Huan, and S. G. Paal. 2018. "Machine learning-based backbone curve model of
- reinforced concrete columns subjected to cyclic loading reversals." *Journal of Computing*
- in Civil Engineering 32 (5).

1161 [61] Tsai, C. H., and D. S. Hsu. 2002. "Diagnosis of reinforced concrete structural damage base on displacement time history using the backpropagation neural network technique." 1162 Journal of Computing in Civil Engineering 16 (1): 49-58. 1163 1164 [62] Jeng, C. H., and Y. L. Mo. 2004. "Quick seismic response estimation of prestressed concrete bridges using artificial neural networks." Journal of Computing in Civil Engineering 18 1165 (4): 360-372. 1166 [63] Song, I., Cho, I. H., & Wong, R. K. 2020. "An advanced statistical approach to data-driven 1167 earthquake engineering." Journal of Earthquake Engineering, 24(8), 1245-1269. 1168